Department of Precision and Microsystems Engineering

3D reflection ptychography using multi-layer Born approach

Jialing Zou

Report no : 2022.029

Daily supervisor: Dr. Yifeng Shao

Supervisor : Prof. Wim Coene, Dr. Wouter Westerveld

Specialisation : MOOM

Type of report : Master thesis
Date : August 4, 2022



Contents

1 Abstract							
2	Introduction 2.1 Wafer metrology	2 2 3 4					
3	$\begin{array}{cccccccccccccccccccccccccccccccccccc$	66 8 12 14 17 23 28 32 33 36					
4	Multi-layer Born model improvements	41					
5	Inverse model for 3D ptychography	nverse model for 3D ptychography 43					
6	Results and discussion 6.1 Single layer reconstruction	47 48 50					
7	Conclusion and outlook 7.1 Conclusions	55 55					
A	Optimal truncation method	60					
В	Diffraction pattern measurements	6 4					
\mathbf{C}	Diffraction pattern predictions	69					

Chapter 1

Abstract

Because of the growing demand for more advanced electric devices, an exponential growth of the number of transistors are supposed to be integrated into a single chip. To manufacture devices in the scale of nanometer cost-effectively, an accurate measurement for lithography process calibrating is necessary. Ptychography is a computational imaging technique which has the potential to serve as a metrology solution for semiconductor devices. It can reconstruct complex-valued permittivity function of an object from an extensive set of measured intensities of the diffraction patterns in the far field. It should be noted that also 2D and 3D a-periodic objects can be measured with this technique. Currently, this technique has been widely used in reconstructing thin and weakly scattering (satisfying the first Born approximation) objects in a transmission geometry (detectors and sources are placed on different sides of the objects). We propose an accurate 3D ptychography multi-layer Born model, and apply it to reconstruct refractive index distributions of semi-conductors. This model slices the sample into thin layers and first Born approximations are applied to each layer sequentially. For a transmission geometry, this model considers both forward scattering effects and backward scattering effects [1], as opposed to normal beam propagation models. For reflection geometry (detectors and sources are placed on the same side of the object), this model collects reflected fields on each layer of the sample and these fields will interact with the object again later together with other upwards fields. This procedure enables detectors arranged in a reflection geometry to gather complete information about the object. We implement the model on the existing ptychography platform based on the auto-differentiation (AD) solvers and manage to reconstruct high-resolution images of 3D objects.

Chapter 2

Introduction

2.1 Wafer metrology

From the mid of the 20th century, the developments of electronic circuit progressed at a rapid rate. With the growing demands for high performance computing, the vast numbers of discrete components and connecting wires inside the electronic devices can no longer suit the portable requirements in modern society. One way to cope with the problem is to integrate multiple components inside a single package. Gordon Moore has predicted that the number of transistors incorporated within a single chip would double every two year [2, 3]. While originally intended as a rule of thumb in 1965, it has become the guiding principle for the industry to deliver ever-more-powerful semiconductor chips. To enable cost-effective lithographic production of such number of high-performance chips,, several key parameters have to be closely monitored during the production process, e.g. critical dimensions (CD) and overlay (OV). Therefore, fast measurements of the structural profile of the nanostructures on the chips is extremely important. By continuing monitoring the quality of the products, lithography machines can calibrate errors dynamically for each wafer. Several measurement techniques have been performed nowadays in nanometer-precision instruments.

- Optical critical dimension metrology (OCD) [4]. Manufacturers now rely on scatterometry for OCD measurements. Scatterometry measures small periodic structures on a wafer or mask. It illuminates the sample with light and collects and analyzes the scattered light to obtain both geometry and material optical properties of the structures. Because it is not image based, scatterometry is not constrained by the so-called diffraction limit, which is caused by imperfections in the lenses or misalignment, but it needs prior information about the structural geometry that is to be measured.
- Scanning electron microscope (SEM) [5]. This is one of the most common used technique for in-line integrated circuit measurements. It uses a finely focused electron beam to scan over the sample. The beam-sample interaction produces secondary and backscattered electrons which are captured by detectors, to determine feature and size information of the object with sub-nanometer-scale resolution.
- Atomic force microscopy (AFM) [6]. AFM is a very-high-resolution type of scanning probe microscopy, with demonstrated resolution on the order of fractions of a nanometer, which is more than 1000 times better than the optical diffraction limit. However, this method suffers

from low throughput and it can hardly satisfy the requirements of the fast manufacturing line.

2.2 Research questions

Apart from these advanced technologies for semi-conductor metrology, there are other more disruptive technologies, e.g. ptychography. Ptychography is a lensless imaging technique for 2D or 3D reconstruction of the image of nanoscale structures. It generates images by processing many coherent interference patterns that have been scattered from an object of interest. Ptychography does not image the object directly but rather indirectly through the solution of an inverse problem via an optimization procedure which compares the measured diffraction patterns and predicted diffraction patterns to find a best fit to be retrieved object and the real object. Fig. 2.1 may help further to illustrate this idea. When an incident wave illuminates an object, the corresponding scattered wave at the far field is collected by a detector. Meanwhile, an arbitrary guess of the object is input to a model, which is capable of simulating the interactions of the field and the object. The output of the model is the corresponding diffraction pattern of the input object. In order to realize the real object, we update the input object iteratively by optimization algorithms. In ptychography, multiple diffraction patterns are measured for different positions of the incident probe, so that neighboring probe positions on the object of interest are partially overlapping. Because the diffraction patterns are unique for any given object, when the differences between the measured patterns and the calculated patterns are small enough so that they can be ignored, we may say that the real object has been successfully reconstructed and in this way, we have measured the key structural features of the chips. The purpose of this thesis is to build both the encoding model, which is supposed to predict the field-material interactions, and the decoding model, which contains the optimization algorithms to update the to be retrieved object.

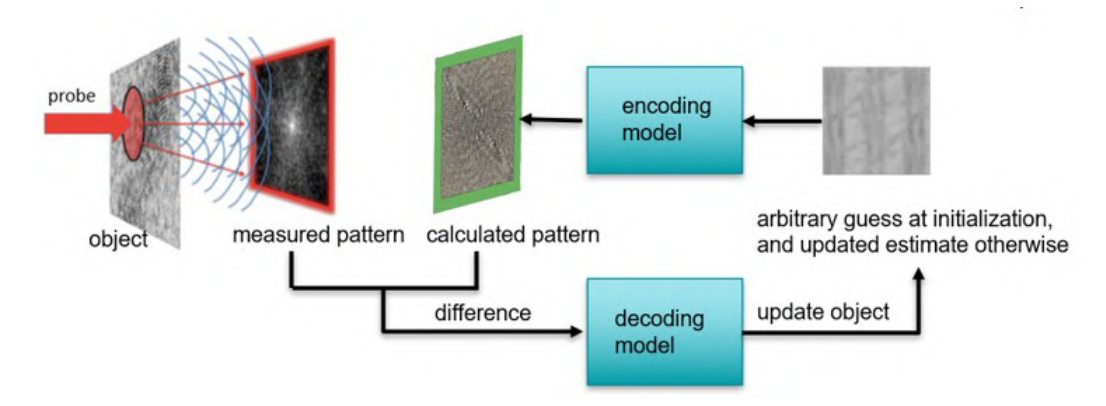


Figure 2.1: Encoding and decoding model in computational imaging

Traditional ptychography is only valid for thin objects, normally not thicker than a few wavelengths of visible lights. This restricts the application of ptychography in many fields. In order to extend the 2D ptychography technique to 3D ptychography, people have come up with some methods [7, 8, 9, 10, 11, 12, 13, 14]. The encoding model which is developed in my thesis in my thesis is the multi-layer first Born (MLB) model. Similar to the multi-slice model, the object will be sliced into thin layers along the incident wave propagation direction and the whole object is obtained by stacking each layer sequentially. However, instead of considering free space propa-

gation between two adjacent layers, the MLB model solves volume integrals to find out the total field at each layer. This method is more rigorous as compared to the multi-slice model and, in addition, it takes backward scattering into account.

As for decoding models, there is a big family of ptychography decoding algorithms. These algorithms are built on iterative optimization methods. By feeding an arbitrary initial complex-valued guess of the object to the algorithm, the algorithm will correct the modulus and phase information of the object with the measured data. The first ptychographic iterative engine (PIE) algorithm became available in 2004 [15], after that, a growing list of alternative algorithms have been demonstrated. Maiden has improved the PIE to ePIE [16], making the algorithm able to reconstruct not only the object function but also the probe function. Later on, ePIE has been demonstrated to work well for X-ray beam [17] and electrons [18]. Unlike the previous PIE family, [19] has demonstrated an optimization framework of ptychography based on automatic differentiation (AD). This AD-based framework is implemented on Tensorflow, a machine learning library. Instead of finding an analytical expression for the gradient of the object and probe functions, AD executes functions as a sequence of elementary arithmetic operations with known derivations, and hence the gradients can be computed automatically by back-propagation following the chain rule. With the benefit from this efficient open-source algorithms, we were able to test the MLB model within the timeframe of this project.

2.3 Thesis outline

In section 3.1, the electromagnetic scattering problem will be formulated. This section derives the important Lippman-Schwinger equation which describes the interactions between the light from the source and the object. By solving this Lippman-Schwinger equation, one may find the total field everywhere both inside and outside of the object. However, due to the unknown total field which is present at both sides of the volume integral equation, it is difficult to solve the equation analytically. Thus we apply the first Born approximation to the Lippman-Schwinger equation to replace the unknown total field inside the integral with the given incident field and by doing so the simplified version of Lippman-Schwinger equation can be solved analytically. Then, based on the first Born approximation applied on the Lippman-Schwinger equation, we introduce the multi-layer Born model in section ??, and then give the theoretical foundation of this model in section 3.3. Also, some tricks have been demonstrated in this section to show how we deal with the computational complexity of these formulas. Things could get more complicated when the background medium is stratified, thus we consider the situation for a multi-layered medium in section 3.4. Then, we verify the multi-layer Born model by comparing the model result with a trustworthy Maxwell solver provided by the Eindhoven University of Technology in section 3.5. The relative errors between these two solvers at each layer are well contained within 0.1. Note that the simulated scatterer has a relative permittivity contrast of 0.066666. This is because the first Born approximation we have applied to the MLB model. It requires the scatterer to has a low relative permittivity contrast $\chi = \frac{n_r^2}{n_b^2} - 1$ much smaller than 1 and for any larger relative permittivity contrast situations, the solver may lead to poor convergence. To prevent this kind of poor convergence, one may reformulate the scattering problem using normal vector fields. However, this requires prior information of the scatterers and the improvement of the results accuracy is limited based on extensive researches. Thus we leave the normal vector fields method to further improvement. Till now, only single wavelength and single sample/probe mode are involved in our MLB model. But in reality, the light source is partially coherent and for high-power EUV source the spectral has a relative large range. Thus multiple wavelength may exit at the same time and influence the scattered field at far

fields. Also, researches have shown that multiple sample/probes are essential to obtain accurate reconstructions. In chapter 4, we improve the model by introducing multi-modes for both samples and probes and multiple wavelengths to make the results more robust. The decoding model will be introduced in Chapter 5. In this chapter, we formulate the reconstruction as an optimization problem. It minimize the difference between the measurements and the MLB model predictions by iteratively updating the scatterer. And by implementing the multi-layer Born model on an open-source automatic differentiation (AD) framework, the derivatives required will be calculated autonomously by the back propagation algorithm. Also, because of the non-linearity of the object function, regularization terms are expected to adjust the model complexity and to prevent the model form overfitting or underfitting. The influence of L1 regularization and total variation (TV) regularization terms on reconstruction will be discussed on this section. Finally, in chapter 6, we use the experimental data provided by the Utrecht university to verify the entire 3D reflection ptychography model, which consists of both the multi-layer Born model and the optimization algorithm. The results are promising when only 4 or less layers are involved. When the number of layers increased, the number of variables also increased. It brings us higher complexities and demands more data to accurately reconstruct the scatterer.

Chapter 3

Multi-layer Born model for 3D ptychography

3.1 Scattering problem formulation

By illuminating the object with a probe, the information of the object is encoded into the wave field. To decode the information, one should first find out the wave field associated with the object. Here we formulate the general model of electromagnetic scattering problem following the procedure in [20] (note that this formulation is more or less the same in all related references): an object is placed in a homogeneous isotropic medium, with a constant relative electric permittivity of ϵ_b . Let Ω represents the space occupied by the object in which the relative permittivity is a function of position, denoted as $\epsilon(\mathbf{r})$. Assume both medium and objects are non-magnetic, so that the relative permeability μ of the whole space is constant. Without loss of generality, we assume it is equals to 1. Now the object is illuminated by a given incident wave, this incident wave will be scattered by the object to all directions. Thus, the total field in this area consists of the known incident wave and unknown scattered field, see Fig. 3.1.

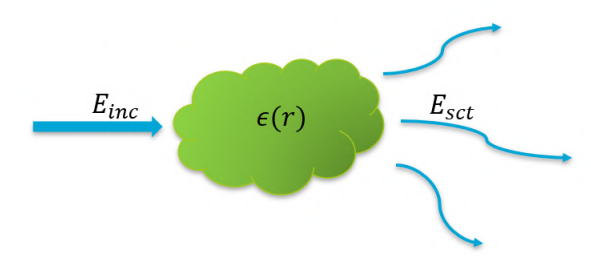


Figure 3.1: General model of electromagnetic scattering problem

Given both incident field and total field satisfy the Maxwell equation, one can derive the expression for scattered field by substracting the incident field from the total field

$$\nabla \times \mathbf{E}_{sct} = i\omega \mu_0 \mathbf{H}_{sct}, \tag{3.1.1}$$

$$\nabla \times \mathbf{H}_{sct} = -i\omega \epsilon_0 \epsilon_b \mathbf{E}_{sct} - i\omega \epsilon_0 (\epsilon(\mathbf{r}) - \epsilon_b) \mathbf{E}_{tot}, \tag{3.1.2}$$

where \mathbf{E}_{sct} , \mathbf{H}_{sct} are scattered electric field and magnetic field, \mathbf{E}_{tot} is the total field. It is obvious that the scattered field satisfies Maxwell's equation when we see $-i\omega\epsilon_0(\epsilon(\mathbf{r}) - \epsilon_b)\mathbf{E}_{tot}$ as an effective current density, \mathbf{J}_{sct} , caused by the induced motions of the bound and free electrons in objects

$$\mathbf{J}_{sct}(\mathbf{r}) = -i\omega\epsilon_0(\epsilon(\mathbf{r}) - \epsilon_b)\mathbf{E}_{tot}.$$
(3.1.3)

To determine the scattered field, one need to solve the Maxwell equations. Eliminate the magnetic field will lead to:

$$\nabla(\nabla \cdot \mathbf{E}_{sct}) - \nabla^2 \mathbf{E}_{sct} = \omega^2 \mu_0 \epsilon_0 \epsilon_b \mathbf{E}_{sct} + \omega^2 \mu_0 \epsilon_0 [\epsilon(\mathbf{r}) - \epsilon_b] \mathbf{E}_{tot}. \tag{3.1.4}$$

For weakly scattering objects, the first term on left-hand side may be discarded, thus we obtain the inhomogeneous Helmholtz equation for the scattered field

$$\nabla^2 \mathbf{E}_{sct} + \omega^2 \mu_0 \epsilon_0 \epsilon_b \mathbf{E}_{sct} = -i\omega \mu_0 \mathbf{J}_{sct}(\mathbf{r}). \tag{3.1.5}$$

The solution to this equation can be written as a convolution of Green's function and source term, which yields:

$$\mathbf{E}_{sct}(\mathbf{r}) = -k_0^2 \iiint_{\Omega} \left[\epsilon(\mathbf{r}_0) - \epsilon_b \right] \mathbf{E}_{tot}(\mathbf{r}_0) G(\mathbf{r} - \mathbf{r}_0) d^3 r_0. \tag{3.1.6}$$

With the expression of the scattered field and the given incident field, we can derive the expression of the total field, which is called the Lippmann-Schwinger equation

$$\mathbf{E}_{tot}(\mathbf{r}) = -k_0^2 \iiint_{\Omega} G(\mathbf{r} - \mathbf{r}_0)(\epsilon(\mathbf{r}_0) - \epsilon_b) \mathbf{E}_{tot}(\mathbf{r}_0) d^3 r_0 + \mathbf{E}_{inc}(\mathbf{r}). \tag{3.1.7}$$

In Cartesian coordinates, components of the electric field do not mix. Each component of the electric field satisfies an inhomogeneous Helmholtz equation. Therefore we derive the scalar form of the Lippmann-Schwinger equation (in [20], the author sticks to the vector expression of electromagnetic fields and uses the Green tensor in his later derivation. For the sake of simplification, we change to the scalar expression from here onwards.)

$$U_{tot}(\mathbf{r}) = -k_0^2 \iiint_{\Omega} G(\mathbf{r} - \mathbf{r}_0)(\epsilon(\mathbf{r}_0) - \epsilon_b) U_{tot}(\mathbf{r}_0) d^3 r_0 + U_{inc}(\mathbf{r}), \tag{3.1.8}$$

where Green's function is given by

$$G(\mathbf{r} - \mathbf{r}_0) = -\frac{e^{ik|\mathbf{r} - \mathbf{r}_0|}}{4\pi|\mathbf{r} - \mathbf{r}_0|}.$$
(3.1.9)

To simplify the total field expression further, here we define the scattering potential $V(\mathbf{r}_0)$ as

$$V(\mathbf{r}_0) = -k_0^2 (\epsilon(\mathbf{r}_0) - \epsilon_b). \tag{3.1.10}$$

Rewriting Eq. 3.1.8 with Eq. 3.1.10 yields:

$$U_{tot}(\mathbf{r}) = \iiint_{\Omega} G(\mathbf{r} - \mathbf{r}_0) V(\mathbf{r}_0) U_{tot}(\mathbf{r}_0) d^3 r_0 + U_{inc}(\mathbf{r}). \tag{3.1.11}$$

By solving Eq. 3.1.11, one can obtain the total electric field both inside and outside of the object. However, note that the unknown total field exist both in left- and right-hand side of the equation, the analytical solution to this integral may be difficult to obtain. To solve this equation, one may replace the total field on the right-hand side of Eq. 3.1.11 with a suitable approximation which could decouple the nonlinear relationship between the scattering potential and the total field.

3.2 Apply Born approximation to solve Lippmann-Schwinger equation

One popular approach to solve the Lippmann-Schwinger equation is to expand the total field on the right-hand side into a Born series

$$U_{tot}(\mathbf{r}) = \sum_{m=0}^{\infty} U_m(\mathbf{r}), \tag{3.2.1}$$

where

$$U_{0}(\mathbf{r}) = U_{inc}(\mathbf{r}),$$

$$U_{1}(\mathbf{r}) = \iiint_{\Omega} G(\mathbf{r} - \mathbf{r}_{0})V(\mathbf{r}_{0})U_{0}(\mathbf{r}_{0})d^{3}r_{0},$$

$$U_{m}(\mathbf{r}) = \iiint_{\Omega} G(\mathbf{r} - \mathbf{r}_{0})V(\mathbf{r}_{0})U_{m-1}(\mathbf{r}_{0})d^{3}r_{0}, m = 1, 2, 3...$$

$$(3.2.2)$$

Normally, people use the First Born approximation (up to m = 1) to approximate the total field. The computation of higher orders is not worthwhile because for normal optical contrast higher order Born series often diverge [20]. The total field is then given by

$$U_{tot}(\mathbf{r}) = \iiint_{\Omega} G(\mathbf{r} - \mathbf{r}_0) V(\mathbf{r}_0) U_{inc}(\mathbf{r}_0) d^3 r_0 + U_{inc}(\mathbf{r}). \tag{3.2.3}$$

By replacing the total field with the incident field on the right-hand side of Eq. 3.1.11, the relation between the scattering potential and the total field is linear, which means this integral is solvable. Electric fields both inside and outside of Ω can be obtained. However, given that only the first two terms contribute to the total field, higher order information is ignored. Thus this approximation is only valid for weakly scattering objects. If the total amount of absorption and phase shift is large, the validity of the first Born approximation is broken down. Recognizing that the first Born approximation only considers single scattering inside the object, one may describe the multiple scattering field-material interactions more accurately by applying the first Born approximation multiple times. In order to do so, the thick object first needs to be divided into many thin layers and each layer is so thin that inside each layer a single scattering model is accurate enough. Thus, one can apply the first Born approximations sequentially at each layer of the object, and by combining all these layers, the multiple scattering effect can then be taken care of. This model is referred to as the multi-layer Born model and was first introduced in [1] by Laura Waller. Similar to the multi-slice method introduced by Maiden et al, they all slice the thick scattering objects into many thin layers along the direction of the incident wave. However, the multi-slice formalism for a thick sample comprises a sequence of phase-gratings and free-space propagators. If a first order Taylor expansion is applied on the phase-grating, a first order Born approximation is obtained. While in the multi-layer Born, one can analytically integrate along the layer thickness in order to get a better analytical result.

Fig. 3.2 describes the geometry of the multi-layer Born model. The lateral cross-section of the object is parallel to the xy plane and the depth of the object expands along the z direction. The permittivity distribution of each thin layer varies in the xy plane, but remains constant along the z direction.

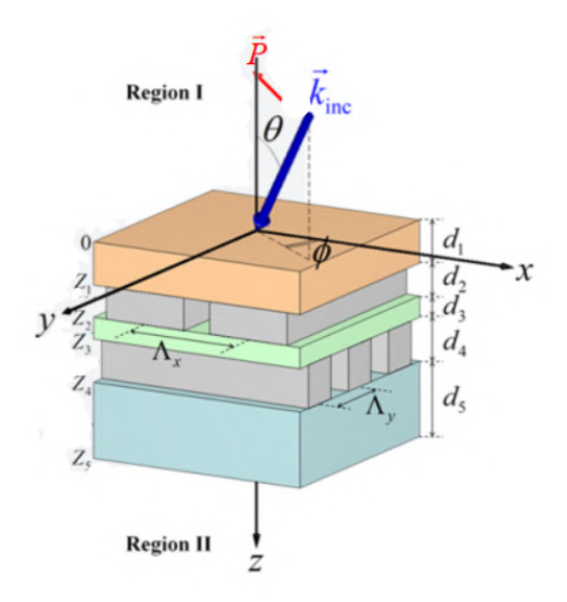


Figure 3.2: The object geometry of the multi-layer Born scattering model [21]

Compared with the multi-slice method which considers only a 2-dimensional transmission/reflection function and a uniform space propagation in the layer, the multi-layer Born model deals with a 3-dimensional object that is constant along the axial direction but varies in the lateral plane. As a result, a volumetric scattering integral, i.e. the Lippmann-Schwinger equation, needs to be used for computing the scattered field. Although we take only the first order approximation of this equation (the first Born approximation), the result of the multi-layer Born model should still be more accurate than that of the multi-slice method when the variation of the scattering potential along the z direction relative to that of the scattering potential in the xy plane is large for the same layer thickness situations.

Given this 3D permittivity distribution which acts as a scattering potential, the scattered field can no longer be obtained by field-material multiplications. Mathematically, a Green's function is the impulse response of an inhomogeneous linear differential operator defined on a domain with specified initial conditions or boundary conditions. This can be understood by the following reasoning: the waves at the top of a layer can be considered as a set of point sources. These point sources interact with the object and propagate forward. The waves at the bottom of the layer is the superposition of all these waves in between. Thus one may find the scattered field analytically by convolving the incident source term and the Green function at each layer. Specifically, the Green's function for finding electromagnetic fields is given by

$$G(\mathbf{r}) = \frac{1}{4\pi r} \delta(r). \tag{3.2.4}$$

Given the convolution between two functions in real space is the multiplication in Fourier space, the calculation will be handled in Fourier space in our codes to decrease the computational load. But similar to the multi-slice method, this multi-layer model is still in the general category of beam propagation methods. As depicted by Fig. 3.2, the incident wave comes from region I and will first interact with the top of the object. Part of the incident wave will be reflected and the other part will be transmitted into the first layer (assume no absorption) and scattered by this

layer. The wave reaches the bottom of the first layer and will further serve as the source wave of the second layer. Similar to the incident wave at the top of the object, it will be divided into two parts, e.g. reflected and transmitted waves. The same process will repeat for every layer and thus in the end, part of the wave will enter region II. In conclusion, one may collect the information of the object from the scattered waves both from region I and region II. To be more specific, if the detector is placed on the same side with the light source (region I in this case), we call it the reflection configuration. And if the detector is placed on the opposite side of the light source (region II in this case), we call it the transmission configuration.

We first take the multi-layer Born transmission model as an example to explain the wave propagation inside the object. Fig. 3.3 demonstrates the xz cross-section of Fig. 3.2 and displays the process of beam propagation and field-material interactions within a three-layer sample of the multi-layer first Born transmission model. The incident field U_{inc} first illuminates the top surface of the object and only part of the field will transmit through the interface and enter the first layer. The fraction of the field that is transmitted at this first interface (at the top of the sample) into the object is determined by the Snell's law and the Fresnel equations. The transmitted field U_{inc}^0 will scatter once at the first layer, and the scattered field at the bottom of the layer may be calculated by the convolution of the total field and the sample scattering potential $V(\mathbf{r})$. Also, because the total field U_{tot}^0 at the bottom of the first layer is the sum of the incident field and the scattered field, one needs to find out the incident field at the bottom of the first layer. The incident field at the bottom of the first layer may be understood as the incident field at the top of the layer U^0_{inc} propagating in a uniform background medium. Summing up the scattered field and the propagated incident field, the total field U_{tot}^0 at the end of the first layer is obtained. By repeating the process all over again for the sequence of consecutive layers till the end of the sample, one is able to obtain the exit field and the diffraction pattern from the wave at the bottom of the sample.

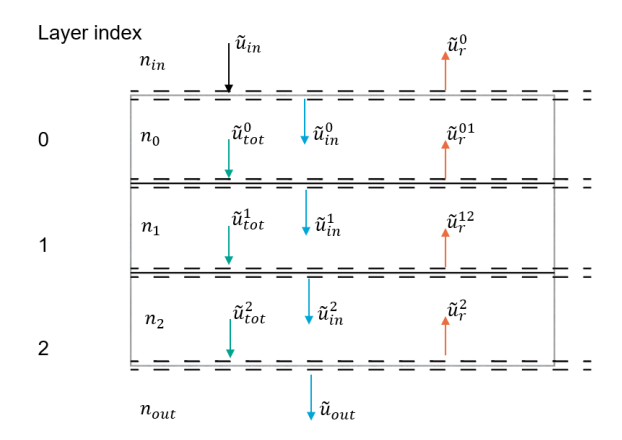


Figure 3.3: Field-material interactions of a three-layer sample in the multi-layer transmission first Born approximation model

In the previous section, we have introduced the physical interpretation of the multi-layer Born model, and now we will give here the mathematical representations of the model. As we have mentioned before, the transmitted fraction of the total field at the bottom of each layer is considered as the incident field at the top of the next layer,

$$U_{inc}^{n+1}(\mathbf{r},0) = U_{tot}^{n}(\mathbf{r},z) * t, (3.2.5)$$

where U_{inc}^{n+1} and U_{tot}^{n} are the incident field at the top of the $(n+1)^{th}$ layer and the total transmitted field at the bottom of the n^{th} layer, respectively. \mathbf{r} is the lateral 2D coordinate in real space. Note that z is a local coordinate. It equals 0 at the top of each layer. t is the transmission Fresnel coefficient which indicates that when the background medium changes from one side to the other side of the given interface, only part of the field will be transmitted to the next medium and the other part of the field will be reflected. The transmission and reflection coefficients are determined by the Fresnel equations. By applying the Fresnel equations, it implies that the tangential components of the electric field are continuous at the interface. In this model, the refractive indices of all background media are real constants as we assume that there is no energy absorption inside the object. And thus the reflectance and the transmittance are supposed to be summing up to one due to the energy conservation law.

The incident field at layer n + 1 will scatter once, so the total field at this layer may be calculated as the sum of the incident field, which propagates in the uniform background medium, and the scattered field, which is scattered by the permittivity contrast (related to spatial variations in refractive indices), as described by the Lippmann-Schwinger equation:

$$U_{tot}^{n+1}(\mathbf{r}, \Delta z) = \mathcal{F}^{-1}\left\{\mathcal{F}\left\{U_{inc}^{n+1}(\mathbf{r}, 0)\right\} * P(\mathbf{r}, \Delta z)\right\} + U_{sct}^{n+1}(\mathbf{r}, \Delta z),\tag{3.2.6}$$

where \mathcal{F} and \mathcal{F}^{-1} represent the Fourier transform and its inverse, respectively. $P(\mathbf{r}, \Delta z)$ is the angular spectrum propagator which indicates how a field propagates from the top of the layer to the bottom of the layer over a distance of the layer thickness Δz . To reduce the number of Fourier transforms performed in the program to accelerate the codes, all calculations are performed in the spatial frequency domain. Therefore, Eq. 3.2.6 becomes:

$$\widetilde{U}_{tot}(\mathbf{u}, z) = \widetilde{U}_{sct}(\mathbf{u}, z) + \widetilde{U}_{inc}(\mathbf{u}, z), \tag{3.2.7}$$

where \widetilde{U} is a short notation for Fourier transforms of fields and \mathbf{u} is a two dimensional spatial frequency coordinate. The incident field at position $z_0 + \Delta z$ in Fourier domain is relatively easy to find as shown in Eq. 3.2.8

$$\widetilde{U}_{inc}(\mathbf{u}, z_0 + \Delta z) = \widetilde{U}_{inc}(\mathbf{u}, z_0) \widetilde{P}(\mathbf{u}, \Delta z). \tag{3.2.8}$$

However, the expression of the scattered field in the Fourier domain requires some heavy derivations (will be demonstrated in Chapter 3.3) and here we only give the final expression of the scattered field at the end of the layer

$$\widetilde{U}_{sct}(\mathbf{u}, \Delta z) = \widetilde{G}(\mathbf{u}, \frac{\Delta z}{2}) \Delta z \mathcal{F} \left\{ V(\mathbf{r}) \mathcal{F}^{-1} \left\{ \widetilde{P}(\mathbf{u}', \frac{\Delta z}{2}) \widetilde{U}_{tot}(\mathbf{u}', 0) \right\} \right\}, \tag{3.2.9}$$

where $\widetilde{G}(\mathbf{u}, z)$ is the Green kernel in the Fourier domain and \mathbf{r} is a two dimensional spatial coordinate in real space. By obtaining total fields at each layer, one may find the total field distribution within the whole thick object.

Our description gets more complicated in the multi-layer Born reflection model, as shown in Fig. 3.4. The whole process may be separated into two parts, a downwards process and an upwards process. In the former, with the fields going downwards, the field-material interactions are similar to those of the transmission model, except that the reflection fields at each layer will be used in later calculations and need to be saved. Also, different from the transmission model where the total field exits the object at the bottom and propagates to the detector, it is the reflected field that needs to be focused on. Given that the detector is on the same side as the light source, the total field has to go back to the top of the sample and then propagate to

the detector in order to obtain the complete information reflected from the object. During the fields going upwards, the major difference between the downwards process is that the incident field of each layer contains both the (upwards) transmitted total field from the last layer and the reflected field saved when the field is going downwards. The Fourier transform of the incident field for each layer during the upwards propagating is given by:

$$\widetilde{U}_{inc}^{n}(\mathbf{u}, z_0) = \widetilde{U}_r^{2nr_{layer}-n-1}(\mathbf{u}, z_0) + \widetilde{U}_t^{n}(\mathbf{u}, z_0), \tag{3.2.10}$$

where nr_{layer} is the number of total layers of the object. The other material-field interactions are similar to that of the downwards interactions.

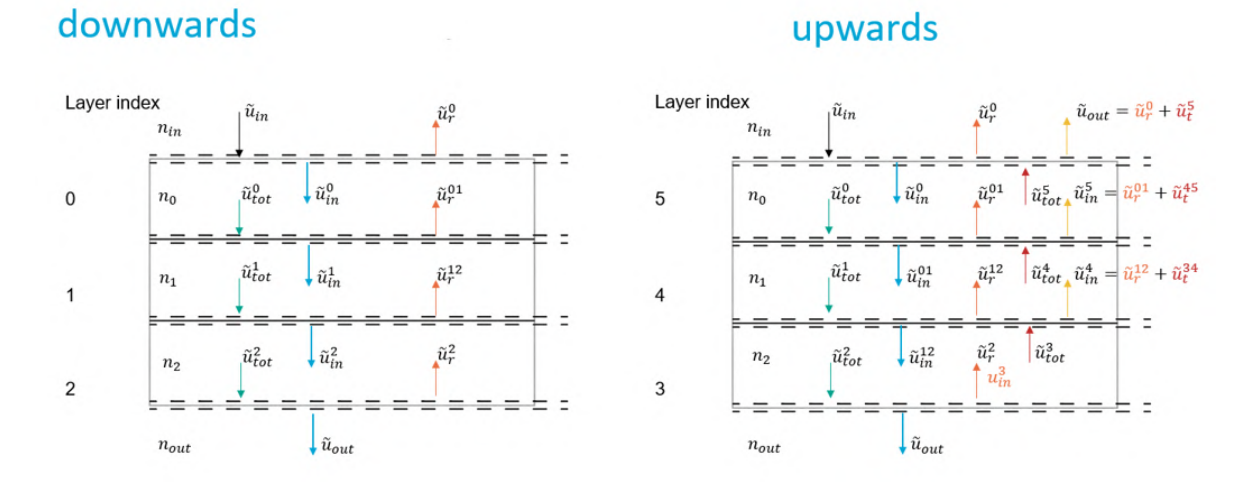


Figure 3.4: Reflection multi-layer Born model field-material interactions in a three-layer sample. The left sub-figure represents the downwards propagation of the total incident field and the right sub-figure indicates the process of waves propagating upwards.

3.3 Multi-layer Born model derivation

The overview picture of the multi-layer first Born model is given in the previous section. Here we will give the theoretical proof of this model.

Suppose that the object is divided into a series of layers along the z direction with the top surface of the object coinciding with the plane at z=0. In each layer, we assume a non-uniform isotropic permittivity distribution $\epsilon(\mathbf{r})$, where \mathbf{r} is the coordinate in the plane perpendicular to the z axis, and a uniform background permittivity ϵ_b . We consider only objects consisting of non-magnetic materials and hence the permeability μ is a constant which equal the permeability of free-space $\mu_0=1$. The scattering potential in each layer is given by

$$V(\mathbf{r}) = k_0^2 (n_b^2 - n^2(\mathbf{r})), \tag{3.3.1}$$

where $n^2(\mathbf{r}) = \epsilon(\mathbf{r})\mu$ and $n_b^2 = \epsilon_b\mu$ are the permittivity contrast of the object and the background, and $k_0 = 2\pi/\lambda$ is the wave number in free-space. Eq. 3.3.1 indicates that the scattering potential varies only in the lateral plane perpendicular to z but remains constant along z. This implies that any variation of the scattering potential along the z axis that is present in the sample, is effectively averaged out along the z-axis within the considered layer.

Now consider a layer with thickness Δz . Recall the Lippmann-Schwinger equation

$$U_{tot}(\mathbf{r}, z) = U_{inc}(\mathbf{r}, z) + \int_0^{\Delta z} \left[\iint G(\mathbf{r} - \mathbf{r}', z - z') V(\mathbf{r}') U_{tot}(\mathbf{r}', z') d\mathbf{r}' \right] dz', \tag{3.3.2}$$

where U_{inc} and U_{tot} are the incident field and the total field, respectively, and $G(\mathbf{r} - \mathbf{r}', z - z')$ is the Green's function that represents the impulse response at (\mathbf{r}, z) from a point source at (\mathbf{r}', z') . Notice that in Eq. 3.3.2, we use a local z coordinate with z = 0 at the top surface of the layer, instead of using a global z coordinate with z = 0 at the top surface of the object.

Solving Eq. 3.3.2 is usually a challenging task because the unknown total field occurs on both sides of the equation. Considering that everywhere in space, the total field U_{tot} is the sum of the incident field U_{inc} and the scattered field U_{sct} :

$$U_{tot}(\mathbf{r}, z) = U_{inc}(\mathbf{r}, z) + U_{sct}(\mathbf{r}, z), \tag{3.3.3}$$

we can apply the first Born approximation to Eq. 3.3.2 by neglecting the scattered field U_{sct} in the integral of Eq. 3.3.2. The result yields the expression for the scattered field:

$$U_{sct}(\mathbf{r}, z) = \int_0^{\Delta z} \left[\iint G(\mathbf{r} - \mathbf{r}', z - z') V(\mathbf{r}') U_{inc}(\mathbf{r}', z') d\mathbf{r}' \right] dz'.$$
 (3.3.4)

In Eq. 3.3.4, the incident field $U_{inc}(\mathbf{r}', z')$ at distance z = z' with respect to the top surface can be obtained by propagating the incident field at the top surface $U_{inc}(\mathbf{r}', 0)$ numerically by using the angular spectrum (AS) method as follows:

$$U_{inc}(\mathbf{r}', z') = \iint U_{inc}(\mathbf{r}', 0)P(\mathbf{r}' - \mathbf{r}, z')d\mathbf{r},$$
(3.3.5)

where $P(\mathbf{r}, z)$ is the AS kernel for a propagation distance of z. By Fourier transforming both sides of Eq. 3.3.4, we obtain

$$\tilde{U}_{inc}(\boldsymbol{\rho}, z') = \tilde{U}_{inc}(\boldsymbol{\rho}, 0)\tilde{P}(\boldsymbol{\rho}, z'), \tag{3.3.6}$$

where $\boldsymbol{\rho}=(u,v)$ is the spatial frequency coordinate of the spatial coordinate $\mathbf{r}=(x,y)$, and $\tilde{P}(\boldsymbol{\rho},z')$ is the AS propagator for z'. Eq. 3.3.6 indicates that in the spatial frequency domain, the Fourier transformed incident fields at z' with respect to the top surface and at the top surface are related to each other by a multiplication by the propagator in Fourier space. In the following derivation, "~" denotes the Fourier transformed variable.

In order to simplify Eq. 3.3.4, we Fourier transform its both sides and we obtain

$$\tilde{U}_{sct}(\boldsymbol{\rho}, z) = \int_0^{\Delta z} \tilde{G}(\boldsymbol{\rho}, z - z') \mathcal{F} \left\{ V(\mathbf{r}) U_{inc}(\mathbf{r}, z') \right\} (\boldsymbol{\rho}) dz', \tag{3.3.7}$$

where \mathcal{F} represents the Fourier transform. Noticing that a multiplication in the spatial domain becomes a convolution in the spatial frequency domain, we can derive that

$$\mathcal{F}\left\{V(\mathbf{r})U_{inc}(\mathbf{r},z')\right\}(\boldsymbol{\rho}) = \iint \tilde{V}(\boldsymbol{\rho}-\boldsymbol{\rho}')\tilde{U}_{inc}(\boldsymbol{\rho}',z')d\boldsymbol{\rho}'$$
$$= \iint \tilde{V}(\boldsymbol{\rho}-\boldsymbol{\rho}')\tilde{P}(\boldsymbol{\rho}',z')\tilde{U}_{inc}(\boldsymbol{\rho}',0)d\boldsymbol{\rho}'. \tag{3.3.8}$$

Substituting Eq. 3.3.8 into Eq. 3.3.7 yields that

$$\tilde{U}_{sct}(\mathbf{r},z) = \int_{0}^{\Delta z} \tilde{G}(\boldsymbol{\rho},z-z') \left[\iint \tilde{V}(\boldsymbol{\rho}-\boldsymbol{\rho}')\tilde{P}(\boldsymbol{\rho}',z')\tilde{U}_{inc}(\boldsymbol{\rho}',0)d\boldsymbol{\rho}' \right] dz',$$

$$= \iint \left[\int_{0}^{\Delta z} \tilde{G}(\boldsymbol{\rho},z-z')\tilde{P}(\boldsymbol{\rho}',z')dz' \right] \tilde{U}_{inc}(\boldsymbol{\rho}',0)\tilde{V}(\boldsymbol{\rho}-\boldsymbol{\rho}')d\boldsymbol{\rho}'. \tag{3.3.9}$$

In Eq. 3.3.9, we define the integration over z' to be a function of not only the spatial frequency coordinates ρ and ρ' , but also of the z coordinate:

$$F(\boldsymbol{\rho}, \boldsymbol{\rho}', z) = \int_0^{\Delta z} \tilde{G}(\boldsymbol{\rho}, z - z') \tilde{P}(\boldsymbol{\rho}', z') dz'. \tag{3.3.10}$$

Now our task is to discuss the computation of $F(\rho, \rho', z)$ which contains only one integral. If it can be written in such a form that the functional dependence on ρ and ρ' can be separated in F, the rest of Eq. 3.3.9, although containing a double integral, can be computed efficiently by using the fast Fourier transform algorithm.

3.3.1 Computation of function $F(\rho, \rho', z)$

Recall that the AS propagator in the spatial frequency domain is given by

$$\tilde{P}(\boldsymbol{\rho}, z) = \exp\left(i2\pi\sqrt{\frac{n_b^2}{\lambda^2} - |\boldsymbol{\rho}|^2} z\right),$$

$$= \exp\left(i\sqrt{k_{0,b}^2 - |\boldsymbol{k}_{\perp}|^2} z\right) = \exp\left[ik_z(\boldsymbol{\rho})z\right],$$
(3.3.11)

where $k_{0,b} = n_b 2\pi/\lambda$ is the wave number in the background medium where the field propagates, $\mathbf{k}_{\perp}(\boldsymbol{\rho}) = 2\pi\boldsymbol{\rho}$ is the wave vector in the plane perpendicular to the z axis, and $k_z(\boldsymbol{\rho}) = \sqrt{k_{0,b}^2 - |\mathbf{k}_{\perp}|^2}$ is the component of the wave vector along the z axis, which is a function of $\boldsymbol{\rho}$. The Fourier transform of the Green's function is given by the Weyl expansion or the angular spectrum expansion:

$$\tilde{G}(\boldsymbol{\rho}, z) = \iint G(\mathbf{r}, z) \exp\left(-i2\pi \mathbf{r} \cdot \boldsymbol{\rho}\right) d\mathbf{r},$$

$$= \frac{-i \exp\left(i\sqrt{\frac{n_b^2}{\lambda^2} - |\boldsymbol{\rho}|^2} z\right)}{4\pi\sqrt{\frac{n_b^2}{\lambda^2} - |\boldsymbol{\rho}|^2}},$$

$$= \frac{-i \exp\left[ik_z(\boldsymbol{\rho})z\right]}{2k_z(\boldsymbol{\rho})}.$$
(3.3.12)

By substituting Eq. 3.3.11 and Eq. 3.3.12 into Eq. 3.3.10, for $z = \Delta z$ we can derive that

$$F(\boldsymbol{\rho}, \boldsymbol{\rho}', \Delta z) = \int_0^{\Delta z} \tilde{G}(\boldsymbol{\rho}, \Delta z - z') \tilde{P}(\boldsymbol{\rho}', z') dz',$$

$$= \int_0^{\Delta z} \frac{-i \exp\left[ik_z(\boldsymbol{\rho})|\Delta z - z'|\right]}{2k_z(\boldsymbol{\rho})} \exp\left[ik_z(\boldsymbol{\rho}')z'\right] dz',$$

$$= \frac{-i \exp\left(ik_z\Delta z\right)}{2k_z} \int_0^{\Delta z} \exp\left[i\left(k_z' - k_z\right)z'\right] dz',$$
(3.3.13)

where we have neglected the spatial frequency coordinate $\boldsymbol{\rho}$ and $\boldsymbol{\rho}'$ in $k_z = k_z(\boldsymbol{\rho})$ and $k_z' = k_z(\boldsymbol{\rho}')$, respectively, and used the condition that $|\Delta z - z'| = \Delta z - z'$ for $z' \in [0, \Delta z]$. Now the result of the integral over z' can be derived analytically as:

$$\int_{0}^{\Delta z} \exp\left[i\left(k'_{z} - k_{z}\right)z'\right] dz' = \frac{1}{i\left(k'_{z} - k_{z}\right)} \exp\left[i\left(k'_{z} - k_{z}\right)z'\right] \Big|_{0}^{\Delta z},
= \frac{1}{i\left(k'_{z} - k_{z}\right)} \left\{\exp\left[i\left(k'_{z} - k_{z}\right)\Delta z\right] - 1\right\},
= \exp\left[i\left(k'_{z} - k_{z}\right)\frac{\Delta z}{2}\right] 2\frac{\sin\left[\left(k'_{z} - k_{z}\right)\frac{\Delta z}{2}\right]}{\left(k'_{z} - k_{z}\right)},
= \exp\left[i\left(k'_{z} - k_{z}\right)\frac{\Delta z}{2}\right] \operatorname{sinc}\left[\left(k'_{z} - k_{z}\right)\frac{\Delta z}{2}\right] \Delta z,$$
(3.3.14)

where we used the following identities in the derivation:

$$\sin\left[\left(k_{z}^{\prime}-k_{z}\right)\frac{\Delta z}{2}\right] = \frac{\exp\left[i\left(k_{z}^{\prime}-k_{z}\right)\frac{\Delta z}{2}\right] - \exp\left[-i\left(k_{z}^{\prime}-k_{z}\right)\frac{\Delta z}{2}\right]}{2i},$$

$$\operatorname{sinc}\left[\left(k_{z}^{\prime}-k_{z}\right)\frac{\Delta z}{2}\right] = \frac{\sin\left[\left(k_{z}^{\prime}-k_{z}\right)\frac{\Delta z}{2}\right]}{\left(k_{z}^{\prime}-k_{z}\right)\frac{\Delta z}{2}}.$$
(3.3.15)

Finally, by substituting Eq. 3.3.14 into Eq. 3.3.13, we can derive that

$$F(\boldsymbol{\rho}, \boldsymbol{\rho}', \Delta z) = \frac{-i \exp\left(ik_z \Delta z\right)}{2k_z} \exp\left[i\left(k_z' - k_z\right) \frac{\Delta z}{2}\right] \operatorname{sinc}\left[\left(k_z' - k_z\right) \frac{\Delta z}{2}\right] \Delta z,$$

$$= \frac{-i \exp\left[i\left(k_z' + k_z\right) \frac{\Delta z}{2}\right]}{2k_z} \operatorname{sinc}\left[\left(k_z' - k_z\right) \frac{\Delta z}{2}\right] \Delta z.$$
(3.3.16)

Recalling that the wave vector \mathbf{k} represents the direction of plane wave propagation, we can thus regard the sinc function in Eq. 3.3.16 as a weighting that depends on the difference between the propagation direction of the plane wave component of the incident field and the scattered field. Consider that any plane wave component of the incident field will be scattered and will be transferred into plane wave propagating in all possible directions. The sinc function indicates that the scattered plane wave that propagates in the same direction of the incident plane wave has the maximum weight 1, and the weight decreases as the difference between the directions of propagation increases following the trend of the sinc function.

Because this sinc function is a 4-dimensional function that depends on the wave vectors of both the incident field and the scattered field, it needs to be simplified such that the dependency on the wave vectors can be separated, e.g. by using the singular value decomposition method (SVD), or it needs to be approximated by a constant 1 provided that either the difference between the wave vectors $k'_z - k_z$ or the layer thickness Δz is sufficiently small. Both approaches will be discussed in the following sections.

Substituting Eq. 3.3.16 into Eq. 3.3.9, we obtain a concrete spatial frequency domain expression for calculating the scattered field at the bottom of a layer given the incident field at the top:

$$\tilde{U}_{sct}(\mathbf{r}, z) = \iint F(\boldsymbol{\rho}, \boldsymbol{\rho}', \Delta z) \tilde{U}_{inc}(\boldsymbol{\rho}', 0) \tilde{V}(\boldsymbol{\rho} - \boldsymbol{\rho}') d\boldsymbol{\rho}',$$

$$= \frac{-i\Delta z}{2k_z} \exp\left(ik_z \frac{\Delta z}{2}\right) \iint \exp\left(ik_z' \frac{\Delta z}{2}\right) \operatorname{sinc}\left[(k_z' - k_z) \frac{\Delta z}{2}\right] \tilde{U}_{inc}(\boldsymbol{\rho}', 0) \tilde{V}(\boldsymbol{\rho} - \boldsymbol{\rho}') d\boldsymbol{\rho}'.$$
(3.3.17)

We shall remember that the z component of the wave vector is given by

$$k_z(\mathbf{\rho}) = \sqrt{k_{0,b}^2 - |\mathbf{k}_{\perp}|^2} = 2\pi \sqrt{\left(\frac{n_b}{\lambda}\right)^2 - |\mathbf{\rho}|^2},$$
 (3.3.18)

where $\rho = (u, v)$ is the spatial frequency coordinate that is related to the spatial coordinate $\mathbf{r} = (x, y)$ by the Fourier transform. Substitute Eq. 3.3.11 and Eq. 3.3.12 into Eq. 3.3.17 to get rid of the exponential term,

$$\begin{split} \widetilde{U}_{sct}(\boldsymbol{\rho},z) &= \iint F(\boldsymbol{\rho},\boldsymbol{\rho}',z) \widetilde{V}(\boldsymbol{\rho}-\boldsymbol{\rho}') \widetilde{U}_{inc}(\boldsymbol{\rho}',0) d\boldsymbol{\rho}' \\ &= \iint \frac{-i\Delta z}{2} \frac{\exp\left[i(\mathbf{k}_z'(\boldsymbol{\rho}') + \mathbf{k}_z(\boldsymbol{\rho}))\frac{\Delta z}{2}\right]}{\mathbf{k}_z(\boldsymbol{\rho})} \operatorname{sinc}\left[(\mathbf{k}_z'(\boldsymbol{\rho}') - \mathbf{k}_z(\boldsymbol{\rho}))\frac{\Delta z}{2}\right] \widetilde{V}(\boldsymbol{\rho}-\boldsymbol{\rho}') \widetilde{U}_{inc}(\boldsymbol{\rho}',0) d\boldsymbol{\rho}' \\ &= \frac{-i\Delta z}{2} \frac{\exp\left[i\mathbf{k}_z(\boldsymbol{\rho})\frac{\Delta z}{2}\right]}{\mathbf{k}_z(\boldsymbol{\rho})} \iint \operatorname{sinc}\left[(\mathbf{k}_z'(\boldsymbol{\rho}') - \mathbf{k}_z(\boldsymbol{\rho}))\frac{\Delta z}{2}\right] \widetilde{V}(\boldsymbol{\rho}-\boldsymbol{\rho}') \exp\left[i\mathbf{k}_z'(\boldsymbol{\rho}')\frac{\Delta z}{2}\right] \widetilde{U}_{inc}(\boldsymbol{\rho}',0) d\boldsymbol{\rho}' \\ &= \widetilde{G}(\boldsymbol{\rho},\frac{\Delta z}{2})\Delta z \iint \operatorname{sinc}\left[(\mathbf{k}_z'(\boldsymbol{\rho}') - \mathbf{k}_z(\boldsymbol{\rho}))\frac{\Delta z}{2}\right] \widetilde{V}(\boldsymbol{\rho}-\boldsymbol{\rho}') \widetilde{P}(\boldsymbol{\rho}',\frac{\Delta z}{2}) \widetilde{U}_{inc}(\boldsymbol{\rho}',0) d\boldsymbol{\rho}', \\ &(3.3.19) \end{split}$$

3.3.2 Apply singular value decomposition to sinc $\left[(k_z'-k_z)\frac{\Delta z}{2}\right]$

The expression of the sinc term in Eq. 3.3.17 is given by

$$S(\boldsymbol{\rho}', \boldsymbol{\rho}) = \operatorname{sinc}\left[(\mathbf{k}_z'(\boldsymbol{\rho}') - \mathbf{k}_z(\boldsymbol{\rho})) \frac{\Delta z}{2} \right]. \tag{3.3.20}$$

The scattering potential $V(\mathbf{r})$ exhibits 2D information of the object (averaged out along the z direction within the layer at hand) that varies in the lateral plane while remaining constant in the axial direction, thus it can be represented by a 2D matrix. The number of elements inside the matrix depends on the sampling grid. Suppose that the scattering potential $V(\mathbf{r})$ is a $N_y \times N_x$ matrix, then the corresponding $S(\boldsymbol{\rho}, \boldsymbol{\rho}')$ needs to be computed for $N_y^2 \times N_x^2$ times for the integration. This calculation requires large computational efforts. However, if we can separate the variables $\boldsymbol{\rho}$ and $\boldsymbol{\rho}'$ from $S(\boldsymbol{\rho}, \boldsymbol{\rho}')$, and write Eq. 3.3.20 as a series of the product of two separate factorized functions each dependent on only one of the coordinates, like:

$$S(\boldsymbol{\rho}', \boldsymbol{\rho}) = \sum_{n} \gamma_n D_n(\boldsymbol{\rho}') Q_n(\boldsymbol{\rho}), \qquad (3.3.21)$$

where γ is a singular-value vector of S and $\gamma_1 \geq ... \geq \gamma_n$. Q_n , D_n are the right and left singular-vectors of the corresponding singular-value, respectively. The computational complexity of the scattered field has decreased to the scale of $N \log N$. Substitute Eq. 3.3.21 into Eq. 3.3.17 to find out the expression of the SVD-based scattered field,

$$\widetilde{U}_{sct}(\boldsymbol{\rho}, z) = \widetilde{G}(\boldsymbol{\rho}, \frac{\Delta z}{2}) \Delta z \iint \operatorname{sinc} \left[(\mathbf{k}_z'(\boldsymbol{\rho}') - \mathbf{k}_z(\boldsymbol{\rho}) \frac{\Delta z}{2} \right] \widetilde{V}(\boldsymbol{\rho} - \boldsymbol{\rho}') \widetilde{P}(\boldsymbol{\rho}', \frac{\Delta z}{2}) \widetilde{U}_{inc}(\boldsymbol{\rho}', 0) d\boldsymbol{\rho}'$$

$$= \widetilde{G}(\boldsymbol{\rho}, \frac{\Delta z}{2}) \Delta z \sum_{n} \gamma_n Q_n(\boldsymbol{\rho}) \iint \widetilde{V}(\boldsymbol{\rho} - \boldsymbol{\rho}') D_n(\boldsymbol{\rho}') \widetilde{P}(\boldsymbol{\rho}', \frac{\Delta z}{2}) \widetilde{U}_{inc}(\boldsymbol{\rho}', 0) d\boldsymbol{\rho}'.$$
(3.3.22)

We can write this formula as a summation of Fourier transform and hence compute by using the FFT algorithm,

$$\widetilde{U}_{sct}(\boldsymbol{\rho},z) = \sum_{n} \widetilde{G}(\boldsymbol{\rho}, \frac{\Delta z}{2}) \Delta z \gamma_{n} Q_{n}(\boldsymbol{\rho}) \mathcal{F} \left\{ V(\mathbf{r}) \mathcal{F}^{-1} \left\{ \widetilde{P}(\boldsymbol{\rho}', \frac{\Delta z}{2}) D_{n}(\boldsymbol{\rho}') \widetilde{U}_{inc}(\boldsymbol{\rho}', 0) \right\} \right\}. \quad (3.3.23)$$

The computational complexity can be further reduced to $n_{max}N\log N$ by truncating the series in Eq. 3.3.23 to the first n_{max} terms. For those singular values that below a certain threshold value, they are too small so that they can be ignored. Extensive literature studies have been executed on methods to truncate high-dimension data to a lower rank [22, 23, 24, 25, 26]. In my graduation project, I have tried the energy accumulation truncation method to reduce the size of $S(\rho', \rho)$.

Energy accumulation method. In this method, I truncate $S(\rho', \rho)$ at rank n which captures 95% energy of it, as shown in Fig. 3.5. The singular values of $S(\rho', \rho)$ are sorted in such order that $\gamma_1 \geq \gamma_2 \geq ... \gamma_j \geq ...$ and plot these singular values in terms of index. The first n terms contain 95% energy of $S(\rho', \rho)$. For those singular values smaller than γ_n are truncated. This is a traditional and convenient way of truncating data. The main purpose of this method is to contain the most information of the data while saving the most of the computing time.

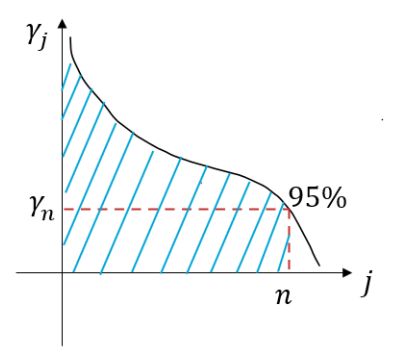


Figure 3.5: Truncated SVD determined by cumulative energy. γ is the singular value vector of $S(\rho', \rho)$. Sort the vector elements in such order that $\gamma_1 \geq \gamma_2 \geq ... \gamma_j \geq ...$ and plot the vector elements, the first n elements contains 95% energy of the vector γ .

Here we use Fig. 3.6 as the permittivity contrast of the object and the background example to show the effect of energy accumulation SVD truncation. Note that the permittivity contrast of the object and the background only has 64×64 pixels, so it looks blurry. The reason for using a low resolution image is that my personal computer(11th Gen Inter Core i7-11800H, NVIDIA GeForce GTX 1650 Ti) does not have enough memory to perform singular value decomposition on a large sized matrix. If the CPU/GPU memory allowed, there are various high-performance SVD solvers available for big data, e.g. PRIMME's GKD basic method [27], fast frequent directions method (FFD) [28]. Also, the magnitudes of Fig. 3.6 are modified to be between -0.1 and 0.1 to represent the low contrast situations given that the multi-layer first Born model is only suitable for weakly scattered objects.

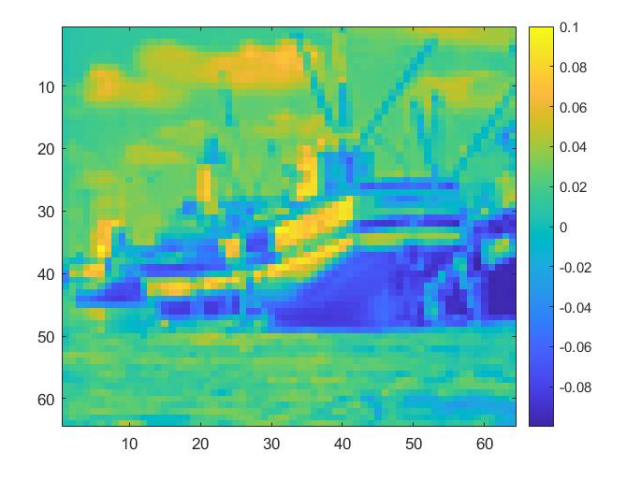


Figure 3.6: Permittivity contrast of the object and the background.

Worth mentioning that the number of modes required to capture 95% energy of $S(\rho', \rho)$ depends on the choices of the lateral plane and the z direction samplings. When the variables are close to zero, the patterns of $S(\rho', \rho)$ will be close to 1 everywhere and the number of modes required

to estimate the $S(\rho', \rho)$ distribution will decrease. Fig. 3.7 shows this trend clearly that with the same lateral plane sampling $(d_x = d_y = 550 \text{ nm})$, the number of modes demanded to capture 95% energy of the $S(\rho', \rho)$ increase when the value of Δz increase. This is because $S(\rho', \rho)$ has a wider range of value distributions and when the variables are away from zero, $S(\rho', \rho)$ may oscillate rapidly around zero. To retain all these features, more modes are demanded.

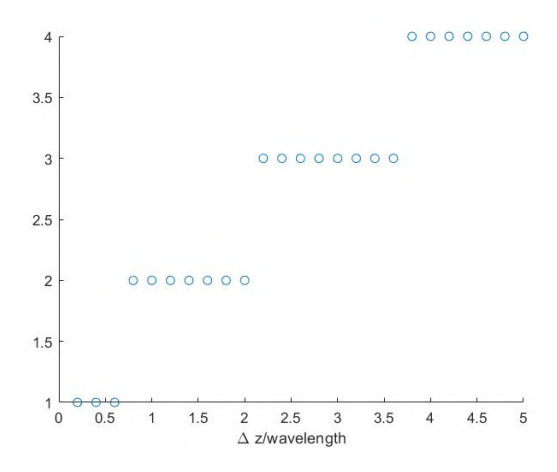


Figure 3.7: The number of modes required to capture 95% energy of the $S(\rho', \rho)$ under different z samplings

In this particular example, Δz is chosen the same as the wavelength, e.g. 550 nm and the lateral sampling interval is equal to $d_x = d_y = 550$ nm.

Since the scattering potential is a 2D matrix with 64×64 elements, the corresponding $S(\rho', \rho)$ has 4096×4096 pixels.

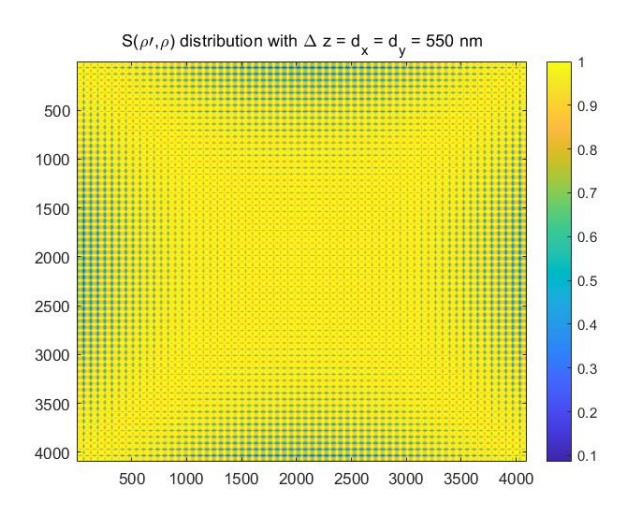


Figure 3.8: $S(\rho', \rho)$ distribution. It depends both on the 2D sampling in the lateral plane, and on the sampling along z. In this example, $\Delta z = d_x = d_y = 550$ nm.

Execution of an SVD on the matrix $S(\rho', \rho)$, reveals Fig. 3.9 which depicts the accumulative energy distribution of the function $S(\rho', \rho)$. It is clear that from the third component onwards, they have little contributions to the final result and thus they can be ignored without influencing the accuracy of the calculation result.

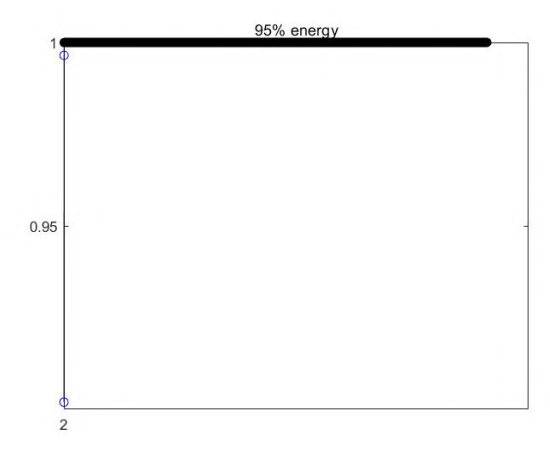


Figure 3.9: Suppose the complete set of modes represents full energy of $S(\rho', \rho)$, the number of modes required to capture 98% energy of $S(\rho', \rho)$ is five.

Fig. 3.9 demonstrates the $S(\boldsymbol{\rho}',\boldsymbol{\rho})$ distribution with only the first two modes retained.

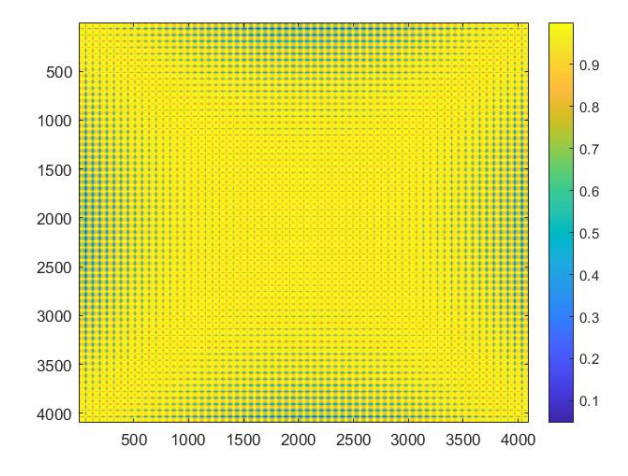


Figure 3.10: The approximated $S(\rho', \rho)$ with only the first two modes.

The scattered field calculated by the first two components of $S(\rho', \rho)$ is shown in Fig. 3.11. When compared with the field computed by complete SVD modes (Fig. 3.12), the magnitude of the truncated SVD version is slightly smaller than that of the full modes. But they are almost the same.

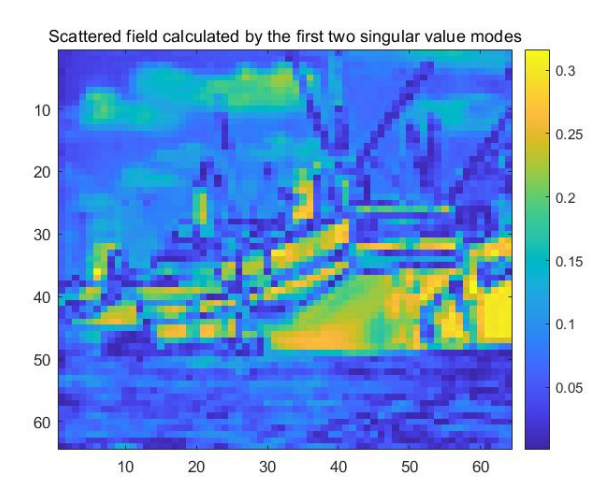


Figure 3.11: Scattered field calculated by the first two modes of $S(\rho', \rho)$

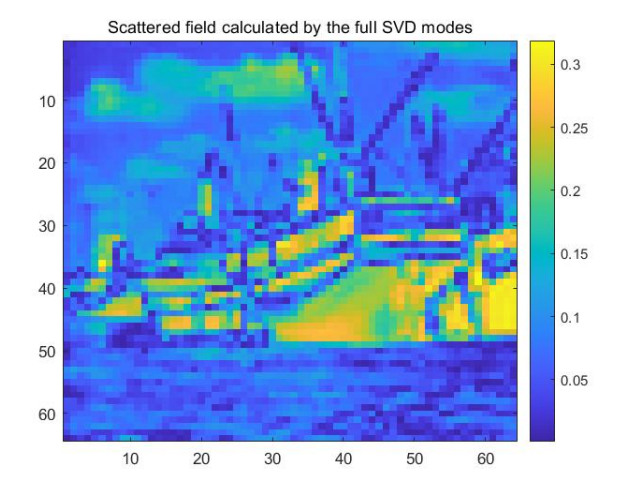


Figure 3.12: Scattered field with the full modes of $S(\boldsymbol{\rho}', \boldsymbol{\rho})$

To quantify the degree of visual and semantic similarity of a pair of matrices (or images), structural similar index measure (SSIM) has been applied. SSIM quantifies image quality degradation caused by processing, such as compression, or by losses in data transmission [29]. In our case specifically, we would like to compare the scattered fields calculated with and without $S(\rho', \rho)$ full SVD modes. The SSIM value is between -1 to 1 with 1 indicating perfect structural similarity. The measure between two matrices x and y is given below:

$$SSIM(x,y) = \frac{(2\mu_x\mu_y + c_1)(2\sigma_{xy} + c_2)}{(\mu_x^2\mu_y^2 + c_1)(\sigma_x^2 + \sigma_y^2 + c_2)},$$
(3.3.24)

$$c_1 = (k_1 L)^2, (3.3.25)$$

$$c_2 = (k_2 L)^2. (3.3.26)$$

In the above equations, μ_x is the average of x, μ_y is the average of y, σ_x , σ_y are the variances of x and y, respectively, and σ_{xy} is the covariance of x and y. c_1 and c_2 are two variables that stabilize the division with a weak denominator, L is the dynamic range of the pixel values. Normally, $k_1 = 0.01$, $k_2 = 0.02$ by default. In our example, the SSIM value between the full modes calculation and the first two mode calculation is almost 1, which means the structural differences between these two scattered fields are small enough to ignore. Fig. 3.13 shows the SSIM map between the two calculated scattered fields.

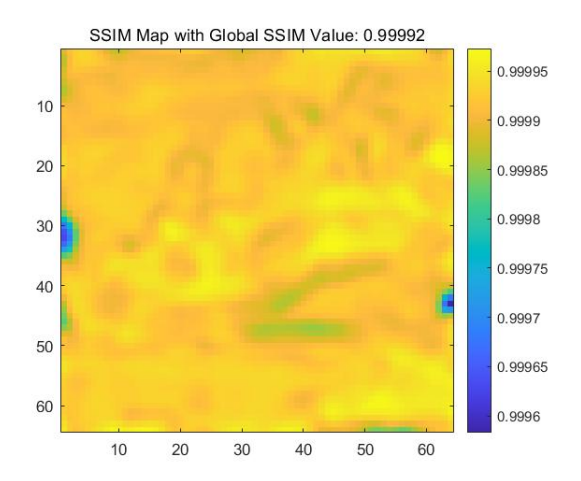


Figure 3.13: SSIM Map with Global SSIM Value: 0.99992

According to the SSIM map, one may find that the low contrast area has SSIM values very close to 1 and the high contrast information has been partially lost. This result may be interpreted in terms of the fact that the detail information is contained in smaller singular value components of $S(\rho', \rho)$. After truncating the data dimensions, the minor or less important features are discarded to decrease the computational load. Due to the similarity of the scattered fields, the truncated results are reliable.

3.3.3 Approximate $S(\rho', \rho)$ to 1 under proper conditions

Although SVD manages to separate the variables ρ' and ρ from the sinc function, and speed up the Green function convolutions using fast Fourier transforms(FFTs), the process of the SVD itself is still computationally intensive. If we can find a way to get rid of the sinc function, the remaining terms inside the integral can be calculated directly by FFTs. Alternatively, we can expand the sinc function in terms of a Taylor series,

$$\operatorname{sinc}(x) = 1 - \frac{x^2}{3!} + \frac{x^4}{5!} - \frac{x^6}{7!} + \dots$$
 (3.3.27)

It shows that as long as the variable x is small enough, the sinc function may be approximated to 1. Notice that the difference between \mathbf{k}_z vectors and the depth between each layer Δz are small, there might be chances that we can simply approximate the complicated sinc function to 1. By approximating $S(\rho', \rho)$ to 1, we can save time because we don't need to perform the SVD and we also need to apply only once the FFT to the computation of the integral in Eq. 3.3.22. The formula for calculating the Fourier transform of the scattered field is then given by

$$\widetilde{U}_{sct}(\boldsymbol{\rho}, z) = \widetilde{G}(\boldsymbol{\rho}, \frac{\Delta z}{2}) \Delta z \mathcal{F} \left\{ V(\mathbf{r}) \mathcal{F}^{-1} \left\{ \widetilde{P}(\boldsymbol{\rho}', \frac{\Delta z}{2}) \widetilde{U}_{inc}(\boldsymbol{\rho}', 0) \right\} \right\}.$$
(3.3.28)

Recall Eq. 3.3.20 which contains two factors that can effect the values of $S(\rho', \rho)$, namely the sampling in the lateral plane and the layer thickness in the axial direction. Now we investigate under which circumstance the sinc function can be approximated as 1.

Lateral plane sampling analysis. According to Eq. 3.3.20, the values of $S(\rho', \rho)$ are dependent on the lateral sampling grid in the spatial frequency domain, which is determined by the sampling in the lateral plane in the spatial domain,

$$N_u = N_x, \tag{3.3.29}$$

$$N_v = N_y, (3.3.30)$$

$$d_u = \frac{1}{N_x d_x},\tag{3.3.31}$$

$$d_v = \frac{1}{N_u d_u}, (3.3.32)$$

where $N_{(x,y,u,v)}$ and $d_{(x,y,u,v)}$ represent the number of sampling points and the sampling interval along the corresponding directions. A smaller sampling interval in the spatial domain leads to higher spatial frequencies in Fourier space so that larger differences between \mathbf{k}_z components can occur. Recall Eq. 3.3.20, larger differences between \mathbf{k}_z vectors may lead to a faster drop of $S(\rho', \rho)$. To visualize the influence of spatial domain lateral plane sampling on the sinc function, we compare the values of the sinc function for various sampling intervals in Fig. 3.14. Because of the central symmetry property of $S(\rho', \rho)$ in the lateral plane sampling, we may only consider sampling along the x-direction for the analysis of this question. Within each subfigure, five different Δz have been demonstrated. We first focus on one Δz , e.g. $\Delta z = 1$ wavelength, the blue line in each subfigure. It is obvious that a smaller spatial domain sampling interval may lead to a faster decrease of the sinc values on the edge of the sampling grid. This is consistent with our analysis that a smaller sampling interval in the spatial domain demands higher spatial frequency components. Although using a coarse grid is beneficial for the approximation of the sinc function, the disadvantage is the poor resolution. In a real experiment, given the illumination source and the camera sensor, the sampling grid is fixed and the only variable free to modify is the layer

thickness Δz . Thus we are supposed to find the proper Δz for a fixed spatial domain sampling grid.

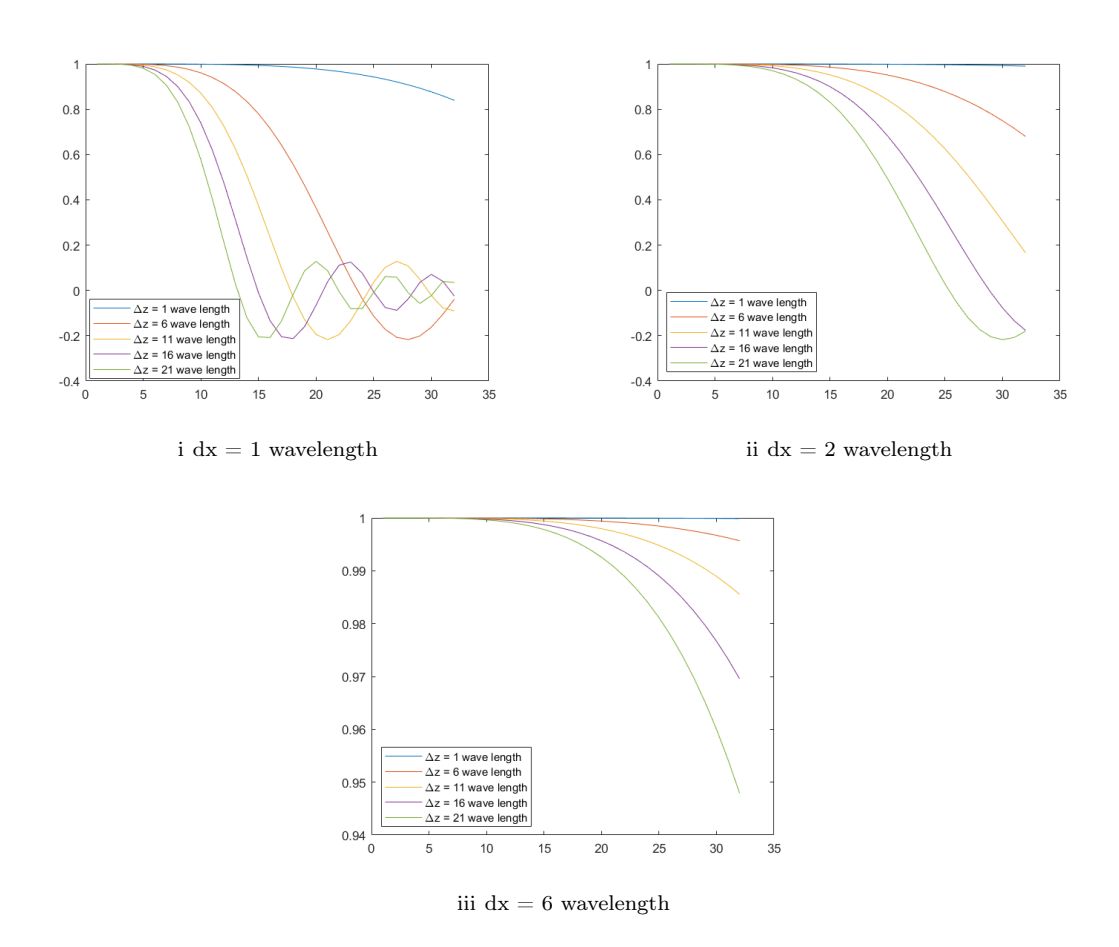
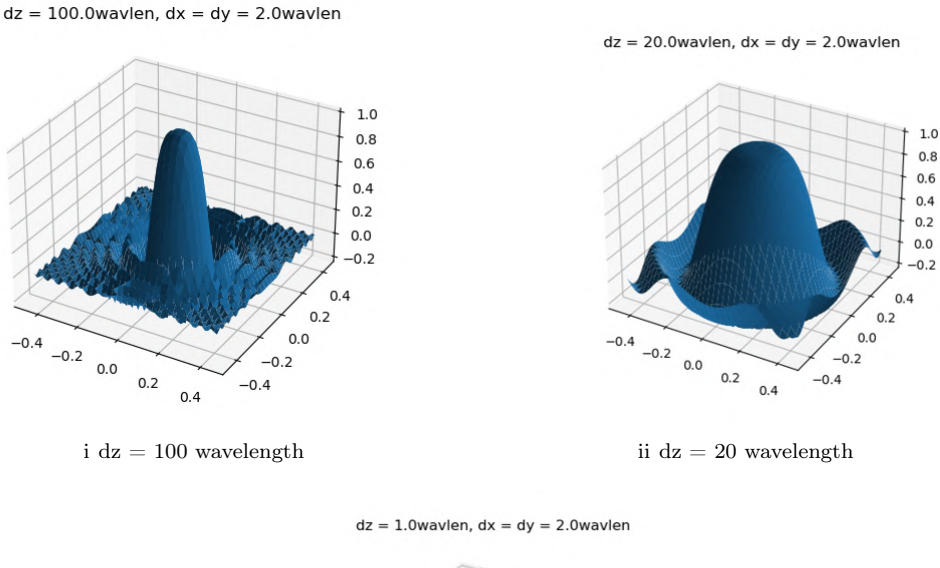
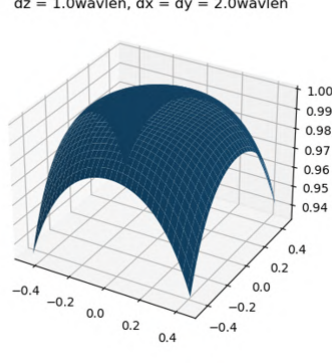


Figure 3.14: $S(\rho', \rho)$ distributions with fixed layer thickness for different spatial domain sampling densities.

z sampling analysis. As we have mentioned before, it is more practical to discuss the selection of Δz when approximating the sinc function to 1. The impact of Δz on the sinc function is straightforward. The larger the Δz , the faster the decrease of the sinc function, as in confirmed by Fig. 3.14. To further investigate the effect of Δz , we plot a 3D figure of the sinc function in Fig. 3.15. It shows the distribution of the sinc function with the same spatial domain sampling interval but with different layer thickness Δz . When $d_x = d_y = 2$ wavelength and $\Delta z = 100$ wave length, the function oscillates around zero near the edge of the sampling grid. Under this circumstance, the sinc function cannot be approximated as a constant. However, when $\Delta z = 1$ wave length, all values of the sinc function are larger than 0.94 so it is sufficiently close to 1. Thus we can draw a conclusion that with a proper Δz , one may approximate $S(\rho', \rho)$ to 1 without losing much of accuracy. Normally, the approximation is closer to the real distribution when Δz becomes smaller. However, for a given object, a smaller Δz represents a larger number of layers and the requirement for computer memories is also increasing. One needs to find a





iii dz = 1 wavelength

Figure 3.15: $S(\rho', \rho)$ distributions with spatial domain sampling interval equal to 2 wavelength

reasonable value which takes both accuracy and computational efforts into account. Thus we have built an optimization algorithm based on the given spatial domain sampling interval and all other related information, such as the background medium refractive index distribution, etc, to determine the maximum Δz when the minimal values of the sinc function are supposed to be larger than a desired threshold. Take the threshold equal to 0.9 and the relative background refractive index equal to 1 as an example, Fig. 3.16 demonstrates the maximum Δz required to make the smallest value of sinc function to be larger than 0.9 for different spatial domain sampling intervals. Table 3.2 provides more accurate values of Δz for several spatial domain sampling intervals.

Benchmarking. To check the validity of the sinc function approximation method, we have taken Fig. 3.6 as an example to calculate the scattered field. In this example, dx and dy are both equal to 1 wavelength and the layer thickness Δz is chosen to be 0.2 wavelength. Fig. 3.17i-3.17ii illustrate the scattered fields with the full SVD modes and a unit constant $S(\rho', \rho)$, respectively.

Table 3.1: Maximum Δz required to have a minimal value of 0.9 of $S(\rho', \rho)$ under different xy plane samplings.

minimal $S(\boldsymbol{\rho}', \boldsymbol{\rho})$	dx/ wavelength	dy/wavelength	dz/wavelength
0.9	1	1	0.27213897
	2	2	1.23413879
	3	3	2.82905247
	4	4	5.06112009

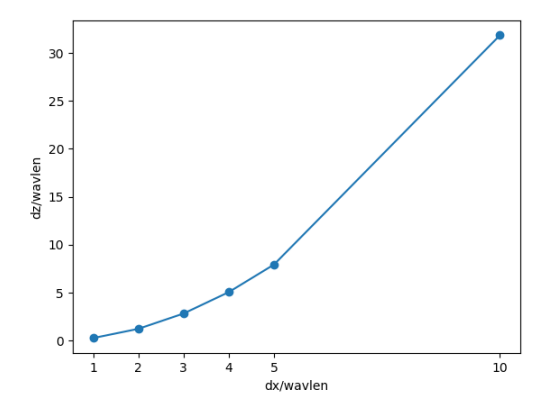


Figure 3.16: Maximum Δz required to have a minimal value of 0.9 of $S(\rho', \rho)$ under different xy plane sampling densities in the spatial domain (with d_x the sampling interval).

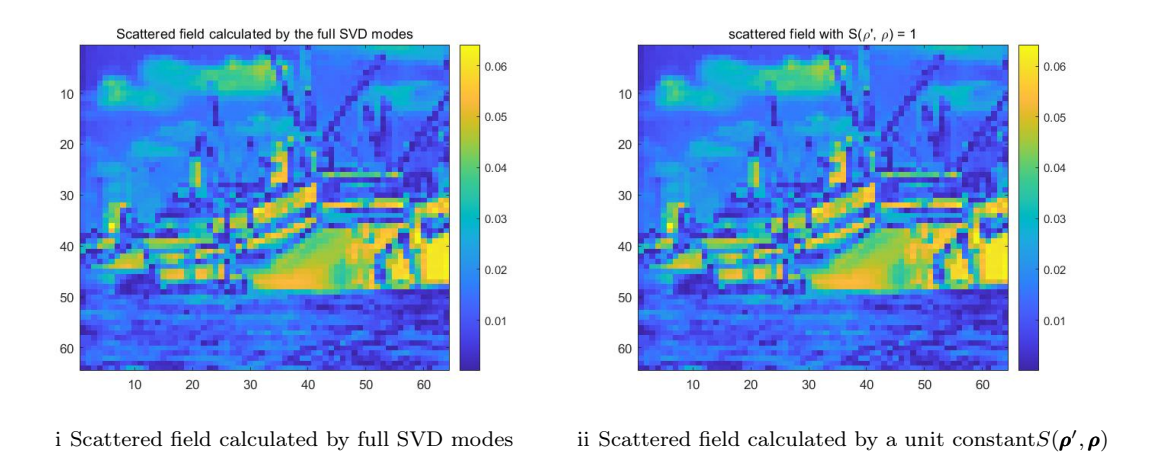


Figure 3.17: Scattered field calculated by full SVD modes and a unit constant $S(\rho', \rho)$, respectively.

According to this figure, we may see that with a unit constant $S(\rho', \rho)$, the amplitude of the scattered field is slightly larger than the amplitude of the accurate field, but the major information of the scattering potential is contained. The SSIM value between these two methods is 1

which indicates that the scattered fields calculated by these two models are structurally similar. Fig. 3.18 displays the SSIM map for the two calculated scattered fields. The lower contrast information is contained to a higher level and the high contrast information is kept in a lower but acceptable range of levels.

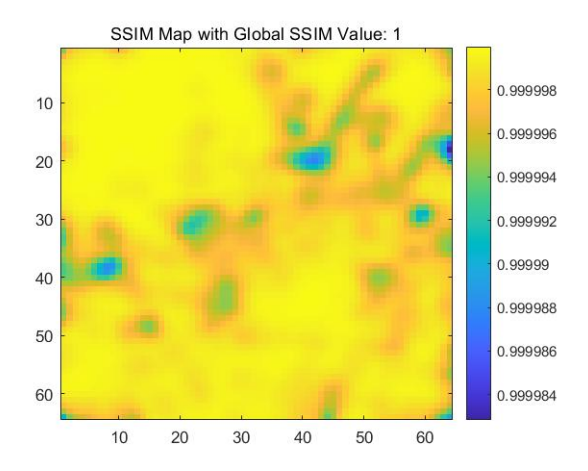


Figure 3.18: SSIM Map with global SSIM value: 1

As long as we have chosen a proper sampling density, the differences of the scattered fields calculated by the SVD truncation method and the unit constant method can be extremely small. Thus we choose to find a small Δz and approximate the sinc function to 1 in the later programming, and this at the low cost of taking thinner layers with smaller Δz .

3.4 Fields in the multi-layered medium

In semiconductor industry, chips are always fabricated in multiple-layered media. Each layer is made of a different material which has different properties in terms of light. Thus an optical wavefront originating from a light source may change its amplitude and phase at the interface between two media. We use the wave vector \mathbf{k} to represent any plane waves. According to Fig 3.19, the relation between the in-plane (xy) wave vector and the incident angle is given by

$$k_x = nk_0 \sin(\theta) \cos(\phi), \tag{3.4.1}$$

$$k_y = nk_0 \sin(\theta) \sin(\phi) \tag{3.4.2}$$

where θ and ϕ are the angles with respect to the z axis and the angle in the xy plane, respectively, $nk_0 = 2\pi/\lambda$ is the wave number and n is the background refractive index.

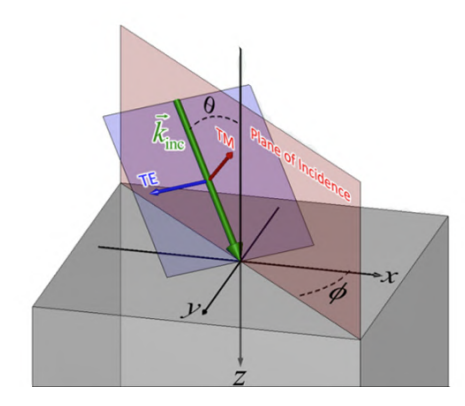


Figure 3.19: The relation between the in-plane (xy) wave vector and the incident angle [21]

For an object consisting of a layered medium, the components k_x and k_y are determined by the incident angle and will not change throughout the entire object due to the Snell's law (since $n\sin(\theta)$ is constant across interfaces). However, the k_z component is different at each layer of the medium. To compute k_z in the i^{th} layer, the dispersion relation in that layer is applied,

$$k_{z,i} = \sqrt{(nk_0)^2 - k_x^2 - k_y^2}. (3.4.3)$$

The change of the wave vector \mathbf{k} through the object is illustrated in Fig. 3.20.

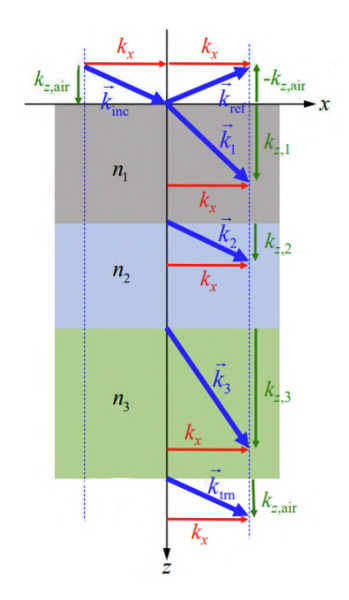


Figure 3.20: k_y , k_y are continuous throughout the object [21]

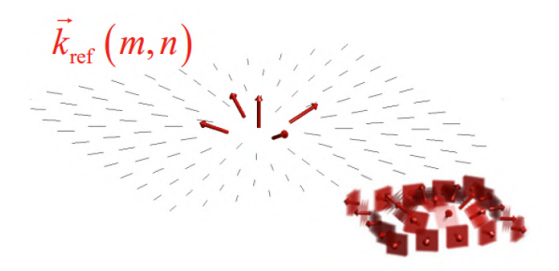
In the Fourier space, the component of the incident field at each spatial frequency represents a plane wave at a particular angle. To perform the calculation fully in the Fourier space, one needs to find the transmission and the reflection Fresnel coefficients for every plane wave at all possible angles. First of all, we need to relate the spatial frequencies to the incident angles at the interface using the following formula:

$$\cos \theta = \frac{k_z}{|k|} = \lambda \sqrt{\left(\frac{n}{\lambda}\right)^2 - |\rho|^2},\tag{3.4.4}$$

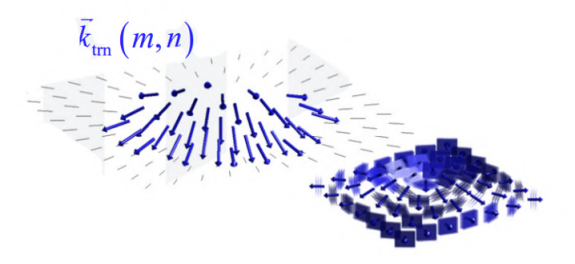
where $\boldsymbol{\rho}=(u,v)$ is the spatial frequency coordinate of the spatial coordinate $\mathbf{r}=(r_x,r_y)$ in the lateral plane perpendicular to the z axis. k_z can be written as a function of spatial frequency $\boldsymbol{\rho}$

$$k_z(\boldsymbol{\rho}) = 2\pi \sqrt{(\frac{n}{\lambda})^2 - |\boldsymbol{\rho}|^2}.$$
(3.4.5)

When $(\frac{n}{\lambda})^2 - |\boldsymbol{\rho}|^2$ is larger than 0, the field will have real k_z , which corresponds to a propagating wave. However, k_z becomes imaginary when the term in the square root is smaller than 0 and the field now corresponds to an evanescent wave that propagates only along the interface. As a result, for these spatial frequencies, the angle with respect to the z axis θ will be set to be zero. Fig. 3.21 visualizes the propagating wave and evanescent waves for both reflection and transmission waves. Each arrow at Fig. 3.21 represents a plane wave at a particular direction. Only those waves represented by red or blue arrows are able to propagate in the space. Those waves represented by the gray arrows are with large angles and hence with imaginary k_z .



i Visualization of the reflected wave spectrum



ii Visualization of the transmitted wave spectrum

Figure 3.21: Visualization of the waves spectrum [21]

After determining the incident angles at the interface, one needs to calculate the transmission and the reflection coefficients. To compute these coefficients, the polarization effect needs to be considered. Polarization is a property of the electromagnetic wave describing the oscillation direction of the electric field vector.

$$\mathbf{E}(\mathbf{r}) = \mathbf{P} \exp(-i\mathbf{k} \cdot \mathbf{r}),\tag{3.4.6}$$

where $\bf P$ is the polarization vector. Different polarization may behave differently in a device. The polarization can be decomposed into two orthogonal directions, e.g. $\bf s$ and $\bf p$. Fig. 3.19 also indicates the information about the relation between incident wave vectors and $\bf s$, $\bf p$ polarization. Both $\bf s$ and $\bf p$ polarization are perpendicular to wave vectors, but $\bf s$ (TE) polarization is orthogonal to the incident plane while $\bf p$ (TM) polarization is inside the incident plane. Due to the different oscillation directions of the electromagnetic fields, the reflection and the transmission properties may change accordingly. Fresnel equations provide the formula to calculate the respective reflection coefficients and transmission coefficients for different polarizations:

$$r_s = \frac{n_1 \cos \theta_1 - n_2 \cos \theta_2}{n_1 \cos \theta_1 + n_2 \cos \theta_2},$$
(3.4.7)

$$r_p = \frac{n_2 \cos \theta_1 - n_1 \cos \theta_2}{n_2 \cos \theta_1 + n_1 \cos \theta_2},$$
(3.4.8)

$$t_s = \frac{2n_1 \cos \theta_1}{n_1 \cos \theta_1 + n_2 \cos \theta_2}. (3.4.9)$$

$$t_p = \frac{2n_1 \cos \theta_1}{n_2 \cos \theta_1 + n_1 \cos \theta_2}. (3.4.10)$$

To calculate the scattered waves accurately inside the object, one may write the incident electromagnetic wave as the superposition of the two waves polarized in orthogonal directions and compute the reflection and the transmission coefficients, respectively.

$$\mathbf{E}(\mathbf{r}) = (E_s \mathbf{s} + E_p \exp(i\delta)\mathbf{p}) \exp(i\theta) \exp(-i\mathbf{k} \cdot \mathbf{r}), \tag{3.4.11}$$

where δ is the phase difference between the two orthogonally polarized waves. Before calculating the scattering problem, one needs to identify the polarization of the incident wave and compute the two waves in orthogonal directions separately. However, this might double the computational load and slow down our program. To simplify the problem, we assume all illumination sources are in the same polarization state and the users are supposed to initialize the state before running the codes.

3.5 Multi-layer Born model verification

To benchmark the MLB model, we first compare the simulation results of a brick sample using both the MLB model and the Maxwell solver provided by the Eindhoven University of Technology(TU/e) [30]. The author of the solver has confirmed the accuracy of the their brick simulation result, so it is safe to consider their result as a ground truth in this case. Given the result provided by the TU/e solver is a three-dimensional matrix consisting of total fields within the whole thick sample, the total field at the top and the bottom will be used to assess the accuracy of the reflection modes and the transmission modes of the MLB model, respectively. The simulated brick has a length of 10μ m in both x and y directions and a thickness of 100μ m in z direction. It has a relative permittivity contrast

$$\chi(\mathbf{r}) = \frac{\epsilon_r(\mathbf{r})}{\epsilon_b} - 1 = 0.066666, \tag{3.5.1}$$

where ϵ_r is the permittivity of the sample and ϵ_b is the permittivity of the background medium. Note that this contrast function is only nonzero within the sample. The lateral cross-section of the contrast function is depicted in Fig. 3.22

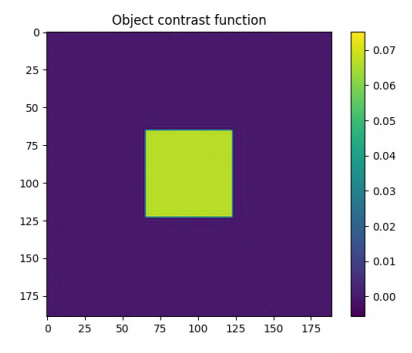


Figure 3.22: Lateral cross-section of the contrast function. The brick is placed at the central area of the sampling area where the relative permittivity contrast is nonzero.

In our simulation, the brick is placed in a stratified space which has relative permittivity contrasts of 0, 2 and 1 respectively. The background medium extends to infinity in the lateral plane. The middle medium has a thickness of 200nm in the z direction and the upper and the lower spaces uniformly extend to the whole space along the z direction. The incident wave illuminates the sample at normal incidence. The amplitude and phase information of the incident wave is illustrated as Fig. 3.23. Other parameters used in the simulations are specified in Table 3.2.

Table 3.2: Parameters used in simulation domain

wavelength	dx	dy	dz	N_x	N_y
$425\mathrm{nm}$	382.5nm	382.5nm	5nm	110	110

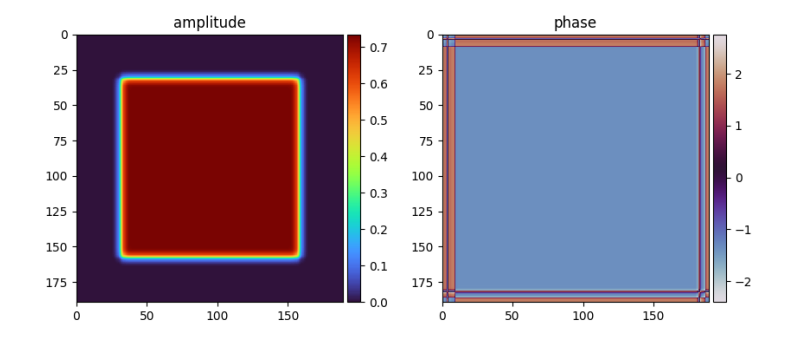


Figure 3.23: Incident field with a normal incident angle. Only the central part where the incident field is nonzero is the simulation domain. The number of pixels in the simulation domain is 110×110 .

3.5.1 MLB model transmission mode

Before comparing the results with the TU/e solvers, we first check the energy conservation of the transmission model. Fig. 3.24 depicts the total energy divided by the incident energy layer by layer inside the object. According to the figure, the energy is well conserved and contained to be 1 all over the place.

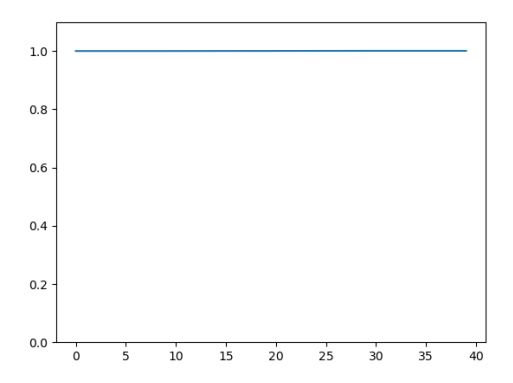


Figure 3.24: The total energy inside the object divided by the incident energy is well contained to be 1 everywhere inside the object. There's no major loss or gain in the materials.

Then we verify the MLB by the TU/e solver. By applying the TU/e Maxwell solver, the total field at the bottom of the brick is depicted in Fig. 3.25. Due to the periodicity in the Fourier domain and properties of the Gabor frame, the electric field outside of the central part is not valid, one may simply ignore the strange pattern around the edge of the figure. Compared with the incident field in Fig. 3.23, it is obvious that the total field is only slightly different from the incident wave after scattering. Because of the weakly scattering property of the brick, the scattered field is much smaller than the incident field and one may hardly observe the scattered field from the total field. In order to observe the scattered field more easily, we crop the central part of the total field at the bottom of the brick and display it in Fig. 3.26. Now that the

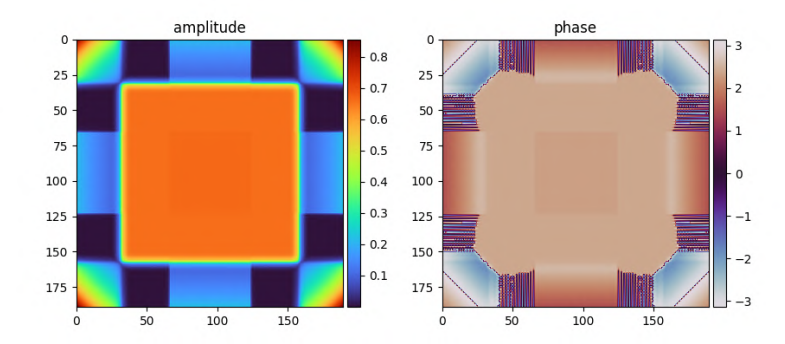


Figure 3.25: Total field at the bottom of the brick

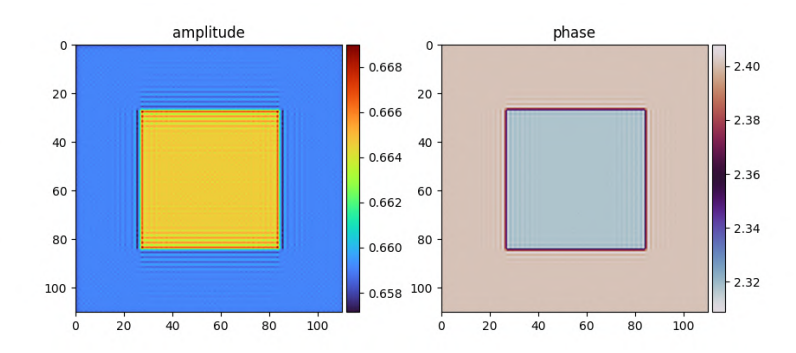


Figure 3.26: Central area of the total field at the bottom of the brick

colourbar has been modified to a smaller scale, the effect due to scattering can be observed more clearly. Due to the usage of the Gabor frames, only central areas of the simulated domain are valid. Thus the simulation grids of the MLB model are equal to the cropped grids of the TU/e solver's. Fig. 3.27 shows the simulation result of the MLB model and as one may observe, the difference between the two models is minor. Both simulations show fluctuations at the edge of the brick and their amplitudes reach its highest value at almost the same locations. This is because of the sudden change of permittivity distributions. Gibb's phenomena may be applied to explain the spikes at the edge of the brick. As is known to all, the total field is the superposition of many plane waves. These plane waves are continuous sine or cosine basis function. When these basis function are used to represent discontinuous functions, e.g. at a material interface, "spikes" appear around each discontinuity. Note that the magnitude of the spikes remains constant no matter how many harmonics are used and it is proportional to the severity of the discontinuity. Thus Fourier space analysis is most efficient for structures with low to moderate index contrast.

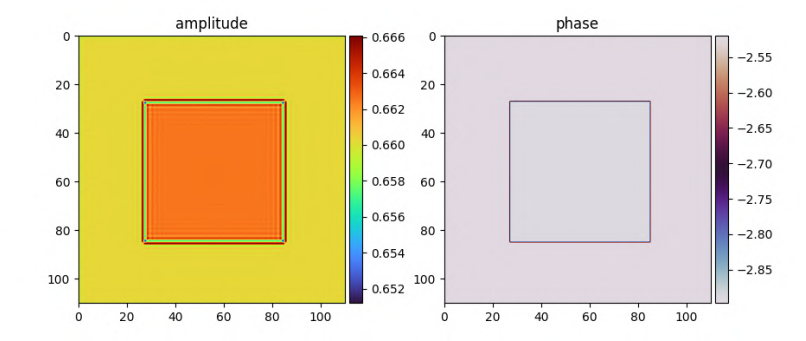


Figure 3.27: Total field at the bottom of the brick MLB model

To quantify the difference between the two models, we apply a root mean square error(RMSE) analysis to the results, which measures the amount of change per pixel. RMSE has non-negative values and a smaller value indicates the greater similarities. Mathematical representation of the RMSE is given as below,

$$RMSE = \sqrt{\frac{\sum_{i=1}^{M} \sum_{j=1}^{N} [A(i,j) - B(i,j)]^2}{M \times N}}.$$
 (3.5.2)

Where M and N are the size of sampling grids and i, j indicate the pixel locations of the fields A, B. The RMSE value of the total field at the bottom of the brick between the two models is 0.0744. For two fields with this small value scales, 0.0744 may assume to be a really small number and the difference between them is acceptable. Fig. 3.28 also gives the RMSE values at each layer for the transmission mode, all RMSEs are well limited within 0.1. Considering that we have ignored the polarization effect in our algorithms, the differences between RMSEs are reasonable. Also, for metrics values in such small scales, we calculate the relative errors to evaluate the prediction performance, as shown in Fig. 3.29.

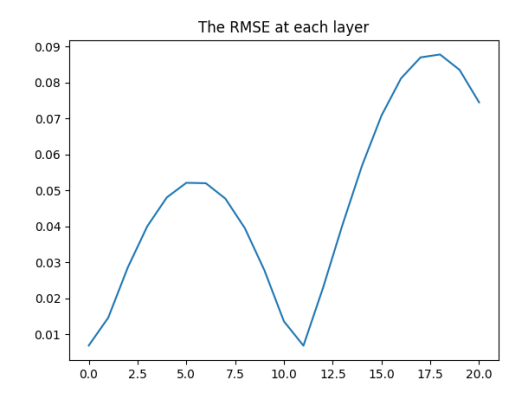


Figure 3.28: Total fields RMSE layer by layer.

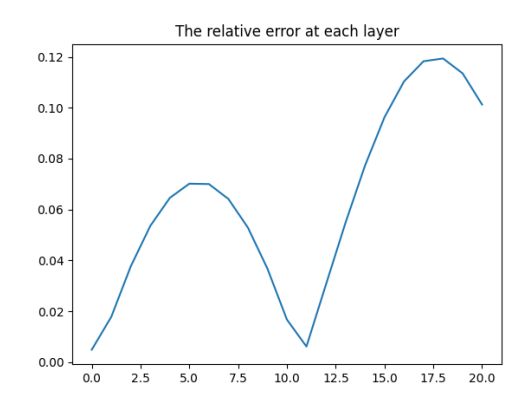


Figure 3.29: Total fields relative errors layer by layer.

3.5.2 MLB model reflection mode

Similar to the MLB model transmission mode, we first check the energy conservation of the reflection mode. The wave power flow of the reflection mode is complicated, we take a two-layer object as an example to explain the energy flow as Fig. 3.30 depicted. One may see from the figure that not only the downwards propagating waves but also the upwards propagating waves are taken into account. Thus to simply the energy conservation verification, we regards the multi-layered object as the whole and only check the wave power exit the object, both from the bottom and the top of the object. If the wave power exit the object summed up to 1, we can believe that this model obey the energy conservation law.

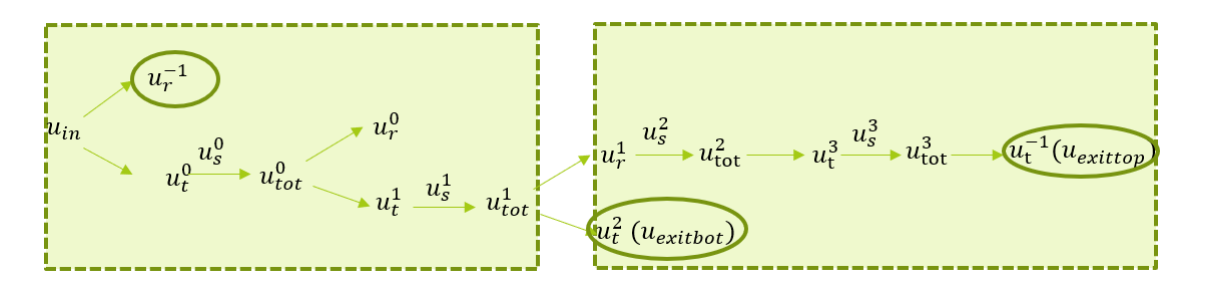


Figure 3.30: Wave energy flow of the incident wave inside the object

According to Fig. 3.30, the incident wave will first be reflected at the top of the object, the wave which enters into the object will interact with the object and part of them will exit the object from the bottom of the object. Remember that there are still waves reflected backwards inside the object and will propagate to the top of the object. Thus there are waves exit the object from the top. To verify the energy conservation law, we check if the following formula stands:

$$\frac{|U_r^{-1}|^2}{|u_{in}|^2} + \frac{|U_t^2|^2}{|u_{in}|^2} + \frac{|U_t^{-1}|^2}{|u_{in}|^2} = 1$$
(3.5.3)

In our simulation, the verified result is 1.0056, which is close to 1. Thus we may conclude that

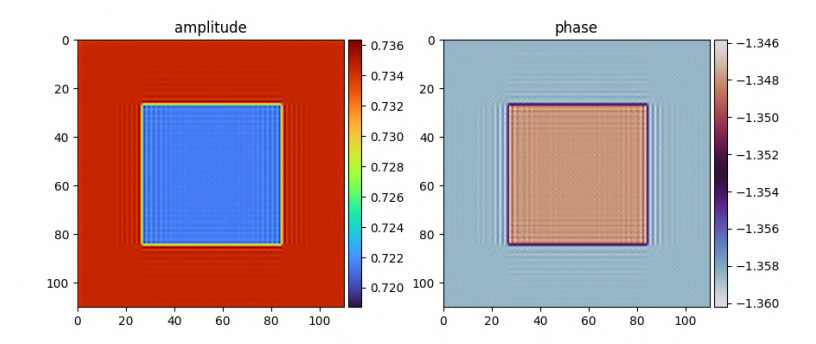


Figure 3.31: Central area of the total field at the top of the brick

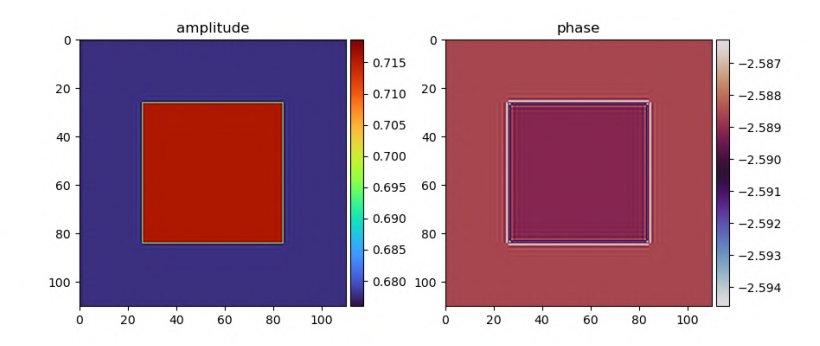


Figure 3.32: Total field at the top of the brick MLB model

the reflection mode does not violate the energy conservation law. Then we check our reflection mode predictions by comparing the total field with the Maxwell solver provided by TU/e.

One may obtain the total field at the top of the sample as well from the TU/e Maxwell solver. With the same sample and the same input field, the total fields at the top of the brick from both models are shown in Fig. 3.31-3.32. The RMSE value between two models is 0.0601, which suggests the results are similar to each other in a high level. As compare with the result of MLB model as shown in Fig. 3.32, both electric fields exhibit a distribution of larger values. The result is reasonable due to the energy conservation law. Only a small part of the waves will be able to penetrate towards the end of the object and large amounts of them are staying at the first several layers. Here we give the RMSEs between the TU/e solver and the MLB reflection mode at all layers. Similar to the transmission mode, the RMSEs are well contained under 0.1 and the relative errors are depicted in Fig. 3.34. A striking difference with the the transmission mode is that the errors at the bottom of the object experience a trend of becoming smaller.

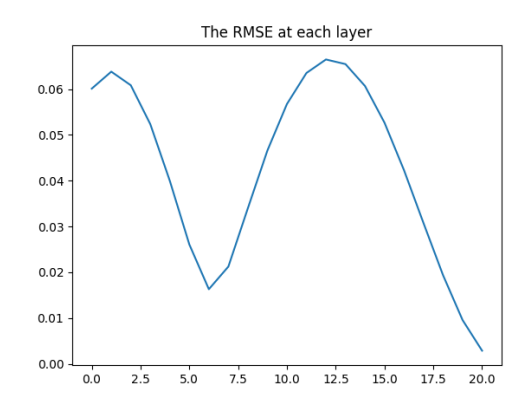


Figure 3.33: Total fields RMSE layer by layer.

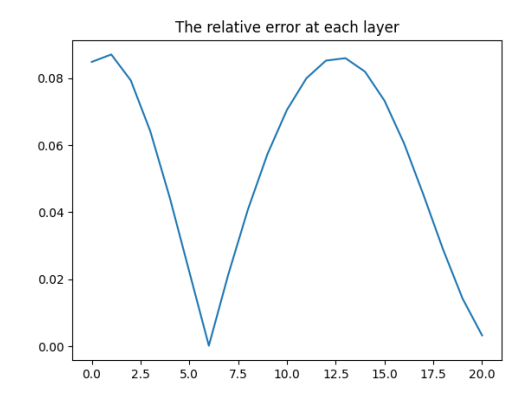


Figure 3.34: Total fields relative errors layer by layer.

The electric field computed by the MLB model is slightly smaller than that of the TU/e solver's, this might result from the choice of Δz . In the MLB model, the Δz term has been taken out of the exponential term and thus has a relative large impact on the final result. A larger Δz will lead to a larger scattered field. The scattered near field is approximately $\frac{\pi \Delta z}{\lambda} [n(\mathbf{r})^2 - n_b^2]$ times of the incident field. This estimation may be easily derived by observing Eq. 3.3.28. The modulation of the Green kernel is about in the order of $\frac{\lambda}{4\pi}$ and the modulation of the terms inside the Fourier operator is approximately in the order of $(\frac{2\pi}{\lambda})^2$. Thus the estimated modulation of Eq. 3.3.28 is about $\frac{\pi}{\lambda} \Delta z [n(\mathbf{r})^2 - n_b^2]$. It is obvious that the selection of Δz may influence the final result a lot. What is worse is that the impact to the final results may be greater when the number of layers doubles in the reflection model (take into account both downwards and upwards propagation), given the errors may be accumulated. Another approach to derive the estimated relation between the incident field and the scattered field is to apply the first Born approximation and thin object approximation to the scattered field. We start from the Helmholtz equation for the total field U and the incident field U

$$k^2 n(\mathbf{r})^2 U(\mathbf{r}) + \nabla U = 0, \tag{3.5.4}$$

$$k^2 n_b U_i + \nabla U_i = 0, \tag{3.5.5}$$

where $n(\mathbf{r})$ is the refractive index as a function of the position and n_b is the refractive index of the background medium. The scattered field $U_s = U - U_i$ satisfies

$$k^{2}U_{s} + \nabla U_{s} = k^{2}(n(\mathbf{r})^{2} - n_{b}^{2})U.$$
(3.5.6)

Hence,

$$U_s(\mathbf{r}) = -k^2 \iiint (n(\mathbf{r})^2 - n_b^2) U(\mathbf{r}_0) G(\mathbf{r}, \mathbf{r}_0) d^3 \mathbf{r}_0,$$
(3.5.7)

with

$$G(\mathbf{r}, \mathbf{r}_0) = -\frac{\exp(ik|r - r_0|)}{4\pi|r - r_0|}.$$
(3.5.8)

We calculate the field far from the object, the Green function $G(\mathbf{r}, \mathbf{r}_0)$ may be approximated as

$$G(\mathbf{r}, \mathbf{r}_0) \approx \frac{\exp(ikr)}{4\pi r} \exp(-i\mathbf{k} \cdot \mathbf{r}).$$
 (3.5.9)

Substituting Eq. 3.5.9 back into Eq. 3.5.7, we get

$$U_s(\mathbf{r}) \approx -\frac{k^2 \exp(ikr)}{4\pi r} \iiint (n(\mathbf{r})^2 - n_b^2) U(\mathbf{r}_0) \exp(-i\mathbf{k} \cdot \mathbf{r}) d^3 \mathbf{r}_0.$$
 (3.5.10)

Now we apply the first Born approximation to Eq. 3.5.10,

$$U_s(\mathbf{r}) \approx -\frac{k^2 \exp(ikr)}{4\pi r} \iiint (n(\mathbf{r})^2 - n_b^2) U_i(\mathbf{r}_0) \exp(-i\mathbf{k} \cdot \mathbf{r}) d^3 \mathbf{r}_0, \tag{3.5.11}$$

and then we apply the thin object approximation to Eq. 3.5.11

$$U_{s}(\mathbf{r}) \approx -\frac{k^{2} \exp(ikr)}{4\pi r} \Delta z \iint [n(x_{0}, y_{0})^{2} - n_{b}^{2}] U_{i}(x_{0}, y_{0}, 0) \exp(-ik(\frac{x}{r}x_{0} + \frac{y}{r}y_{0})) dx_{0}y_{0}$$

$$= -\frac{k^{2} \exp(ikr)}{4\pi r} \Delta z \mathcal{F} \left\{ [n(x_{0}, y_{0})^{2} - n_{b}^{2}] U_{i}(x_{0}, y_{0}, 0) \right\} \left(\frac{x}{\lambda r} \frac{y}{\lambda r}\right).$$
(3.5.12)

In this approximation, we simplify the 3D integral into a 2D integral by taking a small Δz out of the integral. The scattered far field is the Fraunhofer scattered far field of the sample near field. By comparing Eq. 3.5.12 with the Fraunhofer diffraction integral

$$U(x_0, y_0, z_0) = \frac{\exp(ikz_0)\exp(\frac{ik}{2z_0}(x_0^2 + y_0^2))}{i\lambda z_0} \iint U(x, y, 0) \exp[-\frac{2\pi i}{\lambda z_0}(xx_0 + yy_0)] dxdy, \quad (3.5.13)$$

we found that the scattered field at the far field is the Fraunhofer field of

$$-i\pi \frac{\Delta z}{\lambda} [n(x_0, y_0)^2 - n_b^2] U_i(x_0, y_0).$$
 (3.5.14)

Hence, the near field of the object may be written as a multiplication of the incident field by a transmission function t:

$$t(x,y) = -i\pi \frac{\Delta z}{\lambda} [n(x_0, y_0)^2 - n_b^2].$$
 (3.5.15)

This result is approximately the same as the MLB model insofar that both models have a factor of $\frac{\Delta z}{\lambda}$ in front of the incident field. Thus the order of Δz needs to be carefully determined. Normally, scattered fields are only a tenth of the total field and we may chose $\Delta z = \lambda/10$. Also,

this decision of Δz satisfies the requirement for the sinc function when one approximates the sinc function to 1. But stil, the choice of Δz might be tricky and needs to be paid attention to.

Another reason which might cause the difference between these two models is the polarization effect. As mentioned before, the Fresnel coefficients depend on the polarization and the total field is a superposition of p and s polarization. To calculate the electric field accurately, one needs to determine the components of the illuminating source before calculating. The TU/e solver has considered the influence of the polarization while ours model does not for the sake of simplicity.

Chapter 4

Multi-layer Born model improvements

In the previous simulations, only a single wavelength and a single probe/sample mode is calculated for each scanning position, as depicted by Fig. 4.1. However, in reality, the light source is

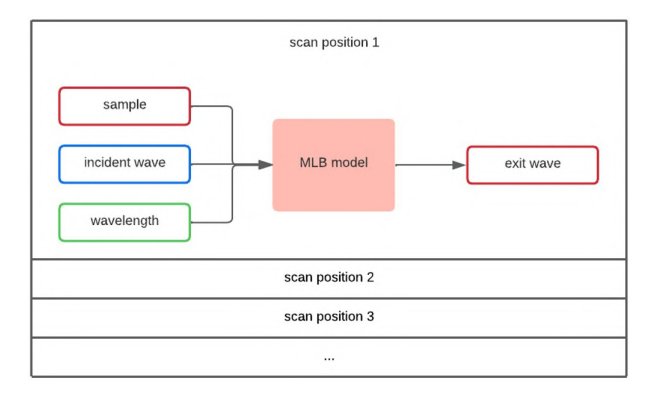


Figure 4.1: Normal workflow of ptychography for each scanning position.

partially coherent and for high-power EUV source the spectral bandwidth has a relative large range [31]. Thus multiple wavelengths may exist at the same time and influence the scattered field at far fields [32]. According to [33], the transverse and longitudinal partially coherent X-rays can be generally formulated by the superposition of multiple modes in both spatial and spectral regimes. Also, [34] indicates that sufficient constraints are required in order to obtain accurate reconstructions due to the mathematical inseparability of multiple sample modes and probe modes which are superimposed to a single set of intensity patterns. Based on these research papers, we increase the complexity of the model by considering multiple wavelengths in the illumination source and multiple modes for both sample and probe thus, making the model more robust to uncertainties. Fig. 4.2 is the flow chart of the model dealing with multi-wavelength and multimodes. Assume the illumination source contains 2 wavelengths, and the sample and the probe have 2 modes, separately. Each time before field-material interactions, the sample needs to be shifted according to the scanning positions. The shifted sample is then cropped into the same

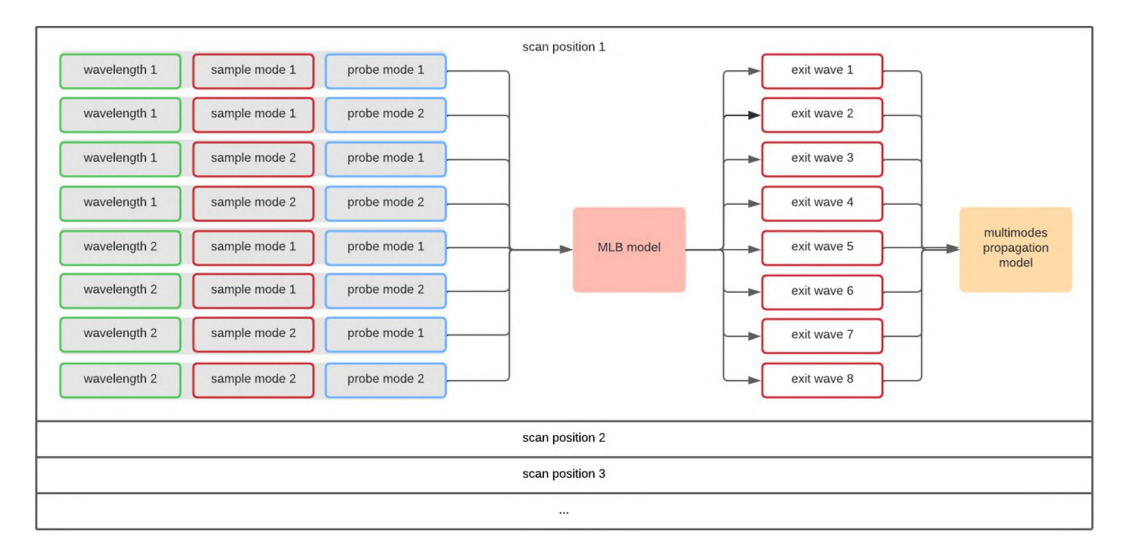


Figure 4.2: Ptychographic workflow of multiple modes and wavelengths

size as the probe size for preparations of the later interactions. Because of the independency of each shifted sample, this parallel process might be designed to run at the same time in GPU to increase the computational speed as long as the computational capacity of the device allows to do so. After that, the high dimensional samples and probes are supposed to lower the dimensions to 2D data, together with the corresponding layer thickness and wavelength entering the MLB model. Note that when considering field-material interactions, all possible wavelengths are calculated one by one and do not mix with each other. However, in the later propagation process, different wavelengths will be assigned to weights and influence the predictions altogether. [35] has illustrated the detail procedure of this polychromatic ptychography technique.

Chapter 5

Inverse model for 3D ptychography

After demonstrating the use of the MLB model, we incorporate it as the forward model of an iterative inverse problem that uses intensity-only images to reconstruct 3D refractive index information. Given the uniqueness of the diffraction patterns of a given incident field and object pair, one may formulate the 3D intensity-only scattering potential reconstruction problem as a optimization problem with an object function $\mathcal{O}(V)$:

$$\min_{V} \mathcal{O}(V) = \sum_{j}^{N} ||U_{j}(V)| - \sqrt{I_{meas,j}}||^{2} + \tau \mathcal{R}(V),$$
 (5.0.1)

where $U_j(V)$ is the current prediction of the MLB model, $\sqrt{I_{meas,j}}$ is the square root of the measured intensity. When feeding the algorithm with an arbitrary initial guess of V to the optimizer (Adam), it will gradually converge to a solution that has the minimum difference between measurements and the predicted model. To solve a minimization problem, one needs to calculate the gradient with respect to the object function to direct the search algorithm. One may compute the gradients of diffraction patterns with respect to objects manually for every specific scattering problems, but it is better to generalize the problem and mitigate the unnecessary excessive laboring. An optimizer based on the frame work of automatic differentiation(AD) in some deep learning API can help solving the nonlinear inverse scattering problem. By using the optimizer based on AD, one can update the object and probe functions without having the analytical expressions of them. The validity and robustness of this AD technique have been proven by extensive number of research papers, e.g. [19, 36, 37]. Thus we built our MLB model under the environment of TensorFlow, an open-source AD framework, to reconstruct the refractive index of the samples. In this inverse algorithm, the scattering potential V is updated sequentially over different sample locations, as opposed to finding averaging values of all gradients from different locations and then refining V. In [38], it has been shown that this approach may not only benefit from a faster convergent speed but also a more accurate result. $\tau \mathcal{R}(V)$ is the regularization term used to adjust the model complexity, preventing the model from overfitting or underfitting. Fig. 5.1 is the workflow of the MLB model embedded in the Tensorflow framework. Based on the flow chart, we can see that wavelength, propagation distance, the complex valued sample function, the complex valued probe function are all to be retrieved variables in the process flow. With a large number of variables, more than enough measured data are required to obtain an accurate and unique solution. The essence of this requirement will be well demonstrated in later reconstructions with multiple layers. Too many variables at once might result in a break down of the inverse solver or a pair of probe and sample reconstruction far from the truth. Such a pair of probe and sample functions does satisfy the low loss function requirement, but do significantly deviate from the real situation. Also, this flow chart indicates the order of derivative chain rules applied in this model. The error will back propagate via CameraLayer, PropLayer, InteractLayer, IlluminateLayer, SourceLayer and SelectLayer sequentially.

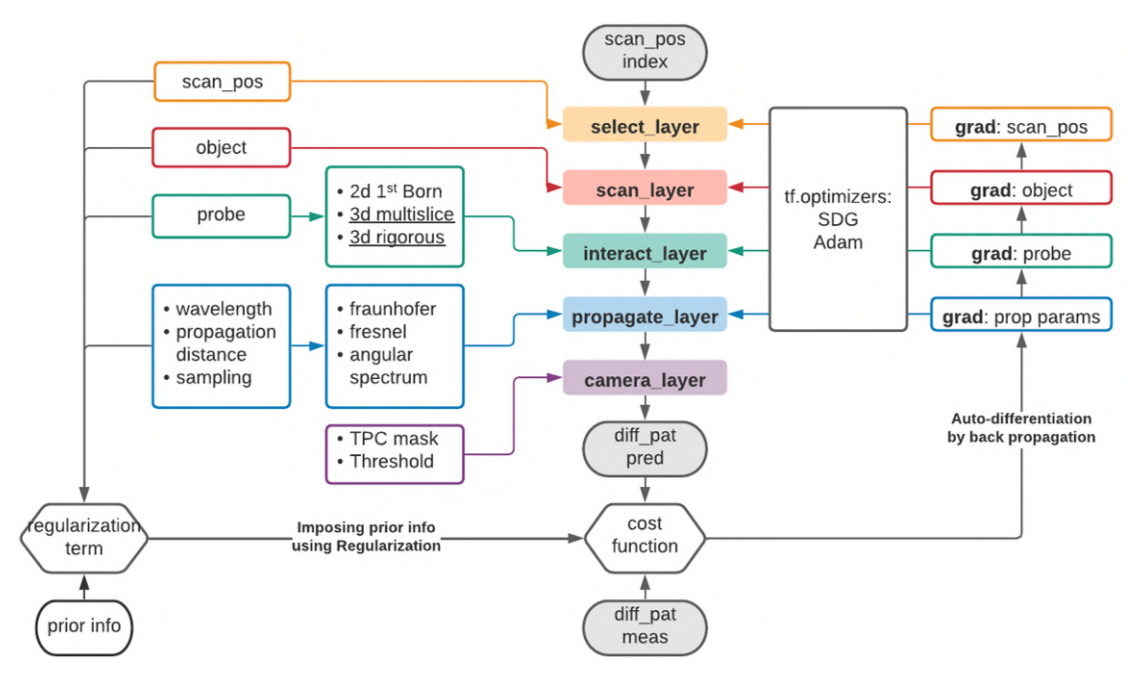


Figure 5.1: MLB model embedded in TensorFlow automatic differentiation framework

What's more, given the multiple wavelengths, sample modes and probe modes settings in the MLB model, several parallel lines of derivations exist in InteractLayer. It increases the computational load but enables the reconstructions to become more robust under circumstances where the current high-power EUV light source has broadband characteristics both in spectral and spatial regimes.

Besides the loss function, regularization term $\tau \mathcal{R}(V)$ is also crucial in the reconstruction process. research paper [39] has demonstrated that the regularization term might improve the quality of reconstructions significantly. If one ignores the regularization term, the model might be too complex and overfit or too simple and underfit, either way giving poor predictions of the scattering potential V. Due to the nonlinearity of the model in this particular case, the regularizer is applied to avoid overfitting. Two kinds of regularizers are applied in this inverse solver, L1 regularization and total variation(TV) regularization. In the L1 regularization technique,

$$Cost = Loss + \lambda \sum_{j}^{M} |W_{j}|, \qquad (5.0.2)$$

it adds absolute the value of magnitude of coefficient as penalty term to the loss function. This technique shrinks the less important feature coefficients to even zero thus, removing some features completely. Given this property, L1 regularization is good for feature selection and denoising.

For the experimental data provided by Utrecht University, the L1 constraint does suppress the background noise well. Fig. 5.2i demonstrates the reconstruction pattern with the L1 regularizer set to 0 and Fig. 5.2ii shows the pattern with a weight term of 10 of the L1 regularization. The only different setting between these two reconstructions is the L1 regularization. The value of the L1 term weight is obtained by trial and error. When we increase the weighted value gradually from 0 to 10, the background noise slowly disappeared. The background edge noise can be observed clearly in Fig. 5.2i while most of the background edge features have been weakened by the L1 regularizer. The contrast between the major features and the less important features are augmented. Also, for a 3D model, the number of features is large, and L1 helps in eliminating the less important ones. However, when we keep increasing the L1 weighting term, the differences between the reconstruction results are too small to observe. As for total variation (TV)

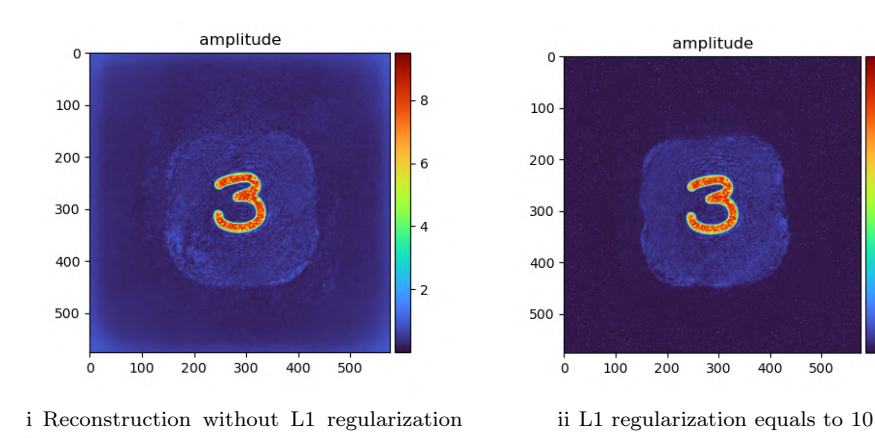


Figure 5.2: Reconstructed pattern with different L1 regularizations

regularization,

$$R(y) = \sum_{i,j} \sqrt{|y_{i+1,j} - y_{i,j}|^2 + |y_{i,j+1} - y_{i,j}|^2},$$
(5.0.3)

where y is a 2D signal, e.g. an image or a 2D complex-valued object field or probe. TV regularization plays a significant role in the denoising process. It based on the principle that signals with excessive details have high total variation, that is, the integral of the absolute loss function is high. According to this fact, reducing the total variation of the signal is capable of removing undesired detail whilst preserving essential structural details [40]. Fig. 5.3 illustrates the importance of TV regularization in that the quality of the reconstructed samples has been improved by removing the speckle noise everywhere behind the major pattern. To arrive the weigh of 20 for the TV regularization term, we have gradually change the weighted values for the TV term from 0 to 30 and see how it influences the reconstructions. With the increasement of the TV term, the speckles behind the major pattern area has been removed to certain extend. However, The differences become minor when we continue increasing the TV term. Thus we choose to display the reconstruction result with a weight of 20 for the TV regularization term. Ref. [41] also points out that in view of better denoising, one needs to identify different noise models including the Gaussian, Impulse, Poisson, Speckle (Gamma), and the mixed Gaussian and impulse noise models. Each noise model may require a specifically tailored TV regularization algorithm in order to get out the best results.

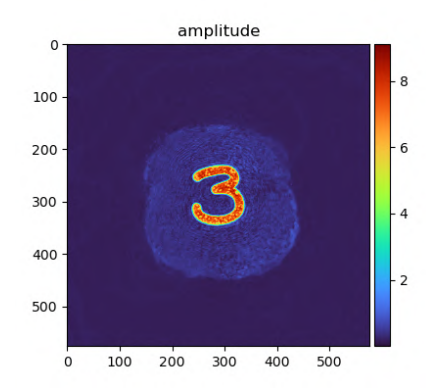


Figure 5.3: Reconstructed pattern with a weight for the TV regularization term equal to 20.

Chapter 6

Results and discussion

To further validate the combination of the encoding model and the decoding model, we use the measurement data from Utrecht University to reconstruct the sample. The sample is a 2mm thick glass with a light absorbing material on the top and only on the central area with a character "3" that can transmit the light. At the bottom of the glass there are some dust particles randomly spread out over the place. Between the pattern 3 and the dust particles is uniform glass. To simulate this thick object, we will slice the sample along the light propagation direction and perform the first Born approximation method at each layer. By reconstructing the refractive index distributions at each of the layer, the total object is obtained. However, as the number of optimization variables increases with the number of layers composing the sample, the accuracy of reconstruction drops down rapidly due to the lack of information. Thus we at first only simulate single-layer objects in section 6.1. Note that our code has been programmed based on the assumption that the sinc function may be approximated to 1, which means the choices of Δz are strict. Thus for a 2 mm sample, there is no way we can simulate it with a single layer only. The purpose here is to demonstrate that even within the safe range of Δz , the selection of Δz can still have large impact on the results. Thus we compare the reconstructions with different Δz in this section. Then we reconstruct the object with multiple layers in section 6.2. Because of the inclusion of the object layers, the number of variables also increased. To successfully reconstruct the object, it requires a higher level of data redundancy and some prior knowledge of the object. Our MLB model works well when the number of layers is below 4 layers, and when more layers involved, the model can become really complicated and the reconstruction may be blurred. One way to improve the bad convergence is to formulate a normal vector field approach. This could be a possible solution given the prior knowledge of nanostructures in ICs that is available since all structures are generated through lithographic imaging of many wafers from the same patterned mask.

6.1 Single layer reconstruction

Fig. 6.1i illustrates a single layer reconstruction result with a Δz of 60nm and Fig. 6.1ii displays the reconstruction which has a Δz of 600nm. Recall Eq. 3.5.15, the magnitude of the scattered field is proportionate to Δz . The larger the Δz , the larger the scattered field is. Comparing these two reconstructions, it is obvious that a larger scattered field provides more details than a smaller one. For a smaller portion of scattered field, there is a huge impact of illumination source on the diffraction patterns. Fig. 6.2 displays the measured diffraction pattern at the first scan position, in comparison to Fig. 6.3i-6.3ii, which demonstrate the predicted diffraction patterns with different layer thickness at scanning position 1. To make the report more compact, the full diffraction patterns are attached in Appendix (B-C). In Fig. 6.3i, the shape of probe is clear to see and the details of the sample are hidden behind the probe pattern. But results can be improved with more optimization iterations. Fig. 6.4i-6.4ii show the reconstruction result with a 60nm Δz after 30 epochs and 100epochs optimizations, respectively. The influence of the probe gets smaller and the image becomes sharper.

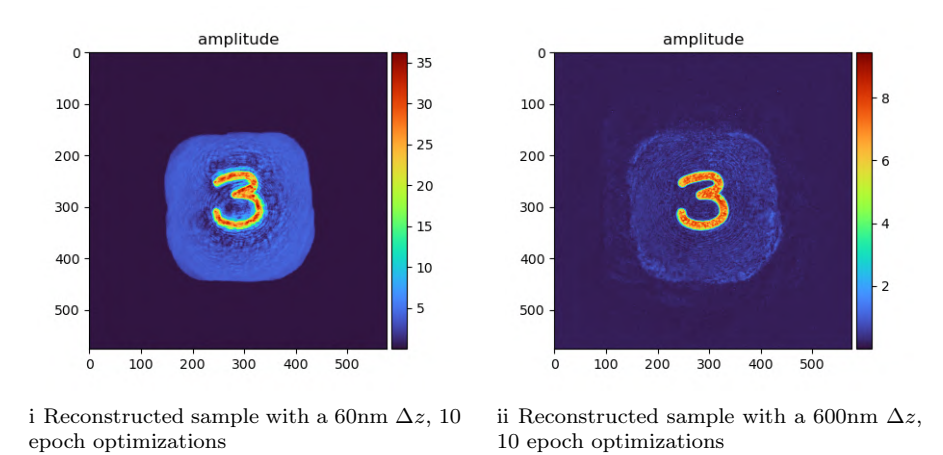


Figure 6.1: Reconstructed pattern with different layer thickness

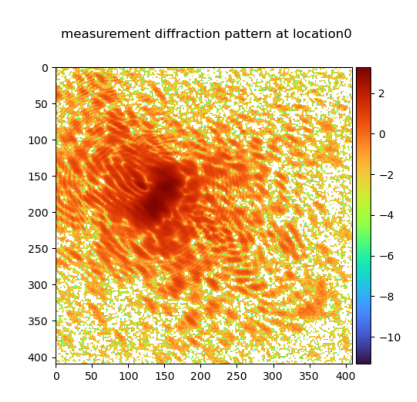
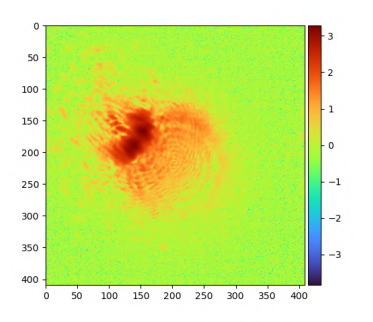
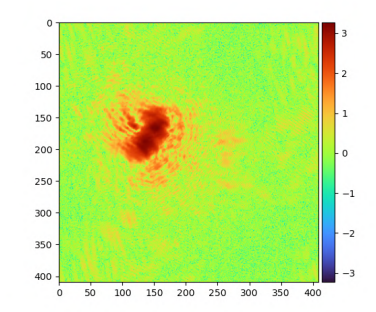


Figure 6.2: Measured diffraction pattern at location 1

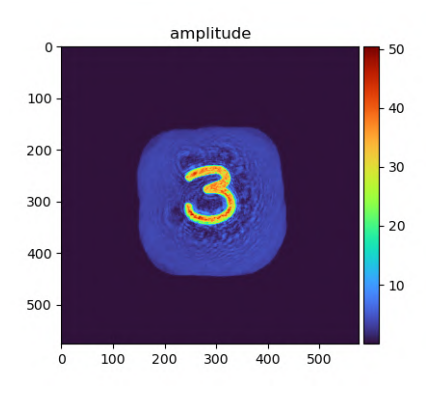


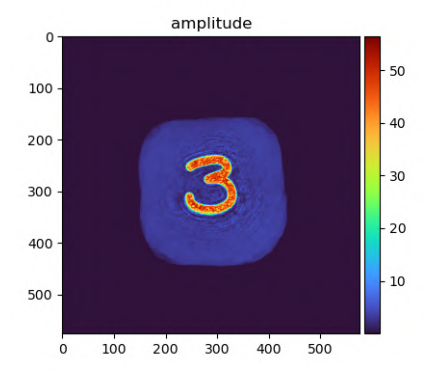


i diffraction pattern prediction at location 1 with a 60nm Δz

ii diffraction pattern prediction at location 1 with a 600nm Δz

Figure 6.3: Diffraction pattern predictions at location 1 with 10 epochs optimizations





i Reconstructed sample with 30 epoch optimizations

ii Reconstructed sample with 100 epoch optimizations

Figure 6.4: Reconstructed pattern with different epochs. Sample has a thickness of 60nm.

6.2 Reconstruction for Multiple Layers

To successfully reconstruct a 3D object, we are supposed to recover the 3D information from 2D measurements. Thus we increase the number of layer composing the object and reconstruct each layer of the object. When the number of layers is large enough, one may safely conclude that the whole 3D object is reconstructed. However, there is a balance between the model complexity and the model accuracy. More layers might be able to better describe the object but it also represents more variables and higher complexity. For the requirement of redundancy in ptychography, a more complex model usually requires more measurement data, which demands a higher level of the experimental setup. What is more, more layers sometimes may bring us accumulated errors and the final result may be far from the truth. For a weakly scattering object, the energy of illumination source is larger than the scattered wave, once the predictions of the probe go offtrack, the sample predictions will change correspondingly. Fig. 6.5i-6.5iv show the object reconstruction with four layers (each layer has a thickness of 60nm).

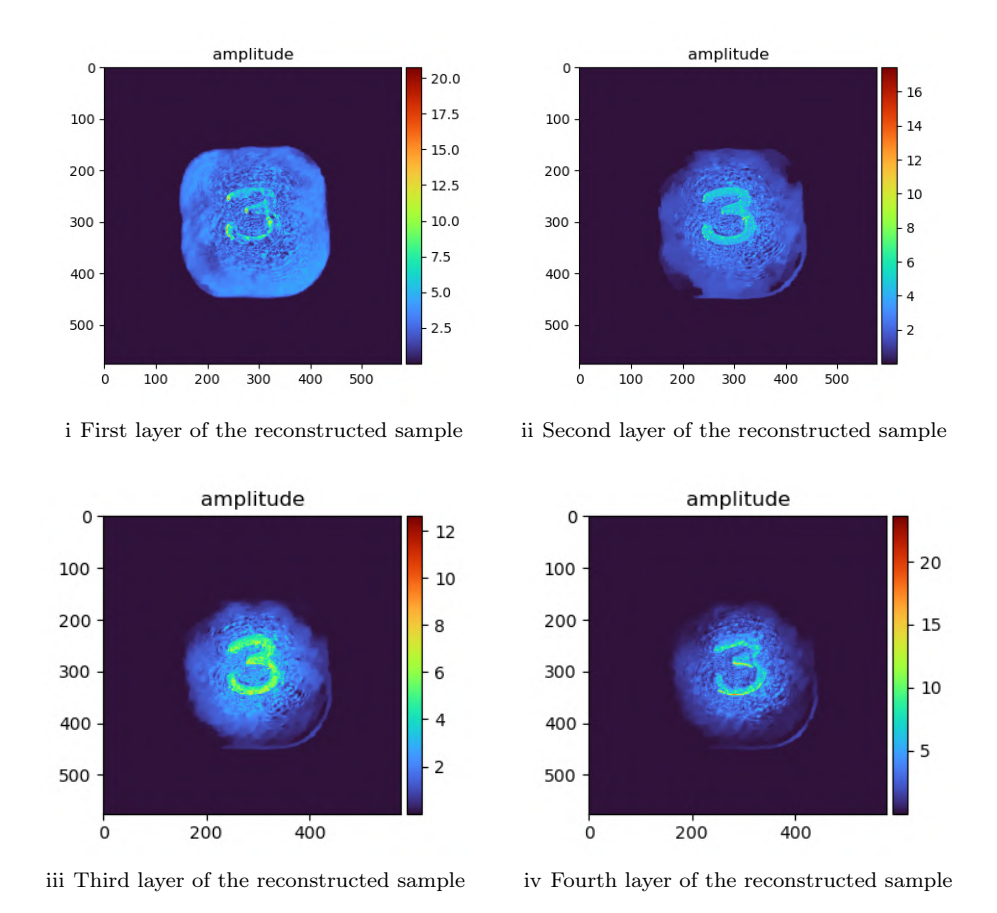


Figure 6.5: Reconstructed pattern of a 4-layers object. Each layer has thickness of 60nm and the patterns are obtained after 100 epochs of optimization

Unlike the single layer reconstruction, all patterns are projected to a 2D plane and one can not tell the spatial information from a 2D projection. But the spatial permittivity distribution can

demonstrated clearly on a four-layers sample reconstruction. On the first layer, the pattern 3 is almost dust free comparing with the later slices and the edges of the pattern 3 has larger values due to the high contrast permittivity distributions of the object on the top of the sample. For the second and the third layers, the contrasts become lower given the uniform permittivity distributions on the middle of the sample. However, due to the existence of dust particles on the bottom of the sample, some dot patterns have shown on the third layer reconstruction. As for the fourth layer, the pattern 3 almost fades away and only patterns inside are clear. Although the patterns are being separated to some extent and very close to the real situations, one has to realize that the process of simulation cannot fully represent the real field-material interactions, given the thickness of the sample is far thicker than our simulation object, which is approximately 2mm. Thus we perform the simulation with a 10-layers sample (each layer has a thickness of 60nm). The reason why we did not perform simulations with hundreds of layers is on the one hand the reconstruction process is time and memory consuming and on the other hand there are already some apparent mistakes appearing with ten layers due to the large number of variables. Fig. 6.6i-6.6x shows the refractive index distributions of the ten-layers sample of each layer. The contrast of the permittivity is relatively low compared with the previous simulations with less layers and the patterns are difficult to recognize.

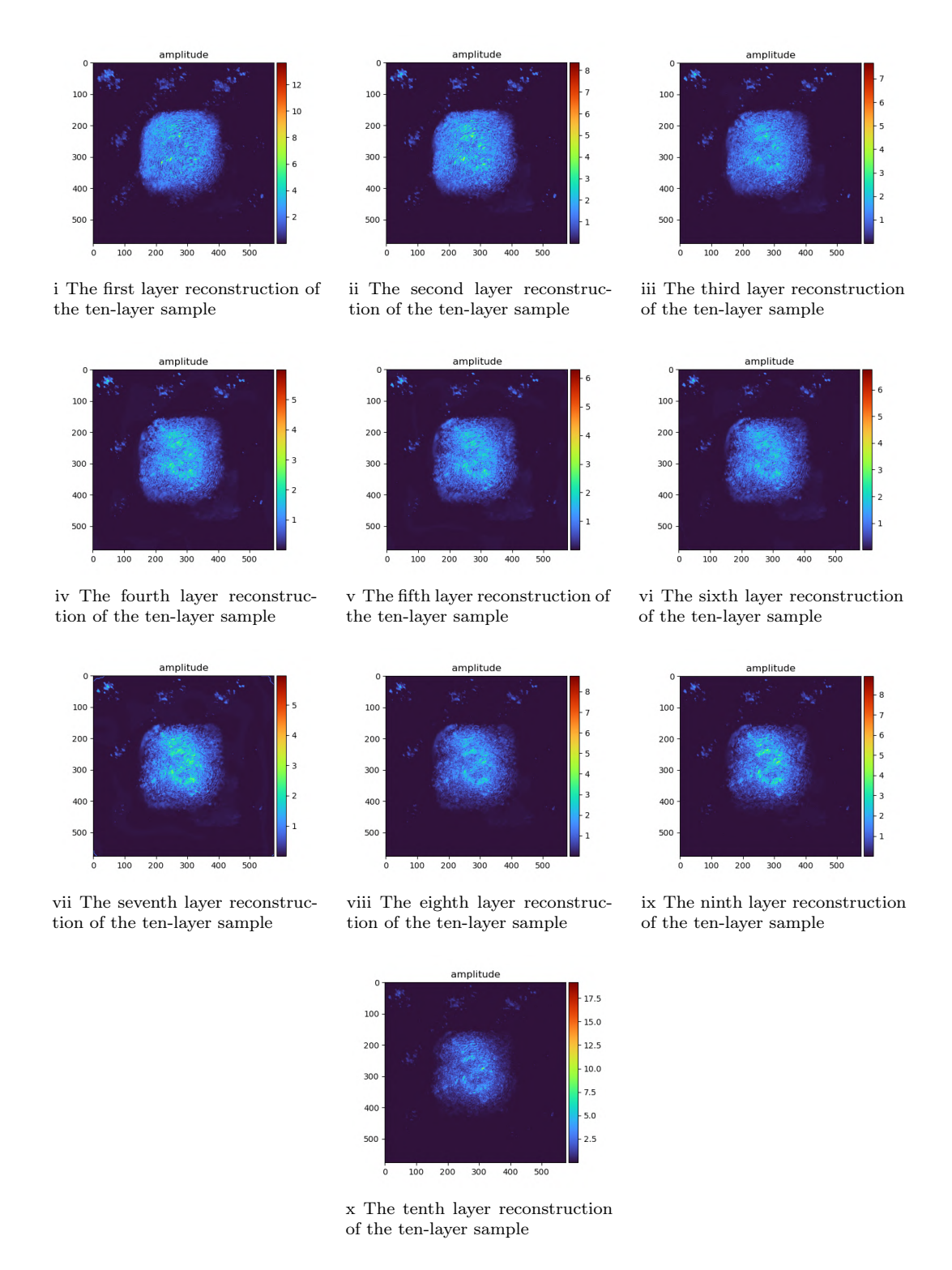


Figure 6.6: Reconstructed pattern of a 10-layer object. Each layer has a thickness of 60nm and the patterns are obtained after 25 epochs of optimizations.

Worth mentioning that not only the sample reconstruction but also the probe reconstruction is far from the real situation. The inaccuracy of the reconstructions partly result from the large amounts of variables and partly because of the limited number of optimization epochs due to restriction in GPU memory. Fig. 6.7i exhibits the reconstructed probe coupled with a ten-layers sample.

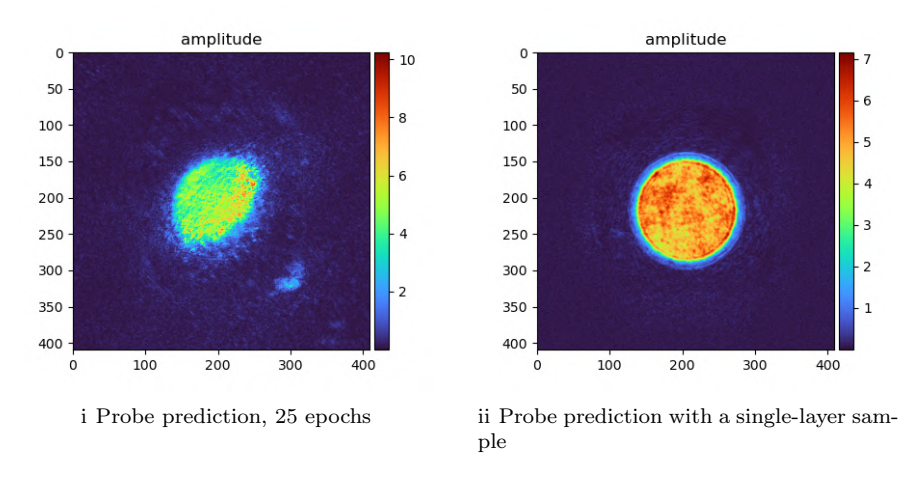


Figure 6.7: Probe predictions

Different from the previous standard circular probe reconstruction (Fig. 6.7ii), this time an irregular probe has been reconstructed. However, even with the wrong probe, the total loss is still low. We may guess that the probe accounts for a large proportion of the total field, the sample will change according to the probe and the coupled changes of the probe and sample lead to a small loss function. This might also imply that lacking of redundancy in ptychography algorithms may lead to multiple solutions. To validate our guess, we have performed a simulation which has a well reconstructed probe (as depicted in Fig. 6.7ii) and the probe variables are set to be untrainable. The corresponding sample reconstruction results are displayed in Fig. 6.8i-6.8x. Although the patterns are still blurry, the sense of layering has been revealed. What is more, the dim patterns in the middle of the layers might arise because that the sample itself has a pure glass in the middle. If we increase the number of iterations, the reconstruction results might be even better. Apart from the number of variables which influences the reconstruction result, the probe size might effect the results as well. To obtain the diffraction patterns, the illumination sources are required to be coherent. If the probe size is too large, there will be only partial interference between exterior parts of the probe.

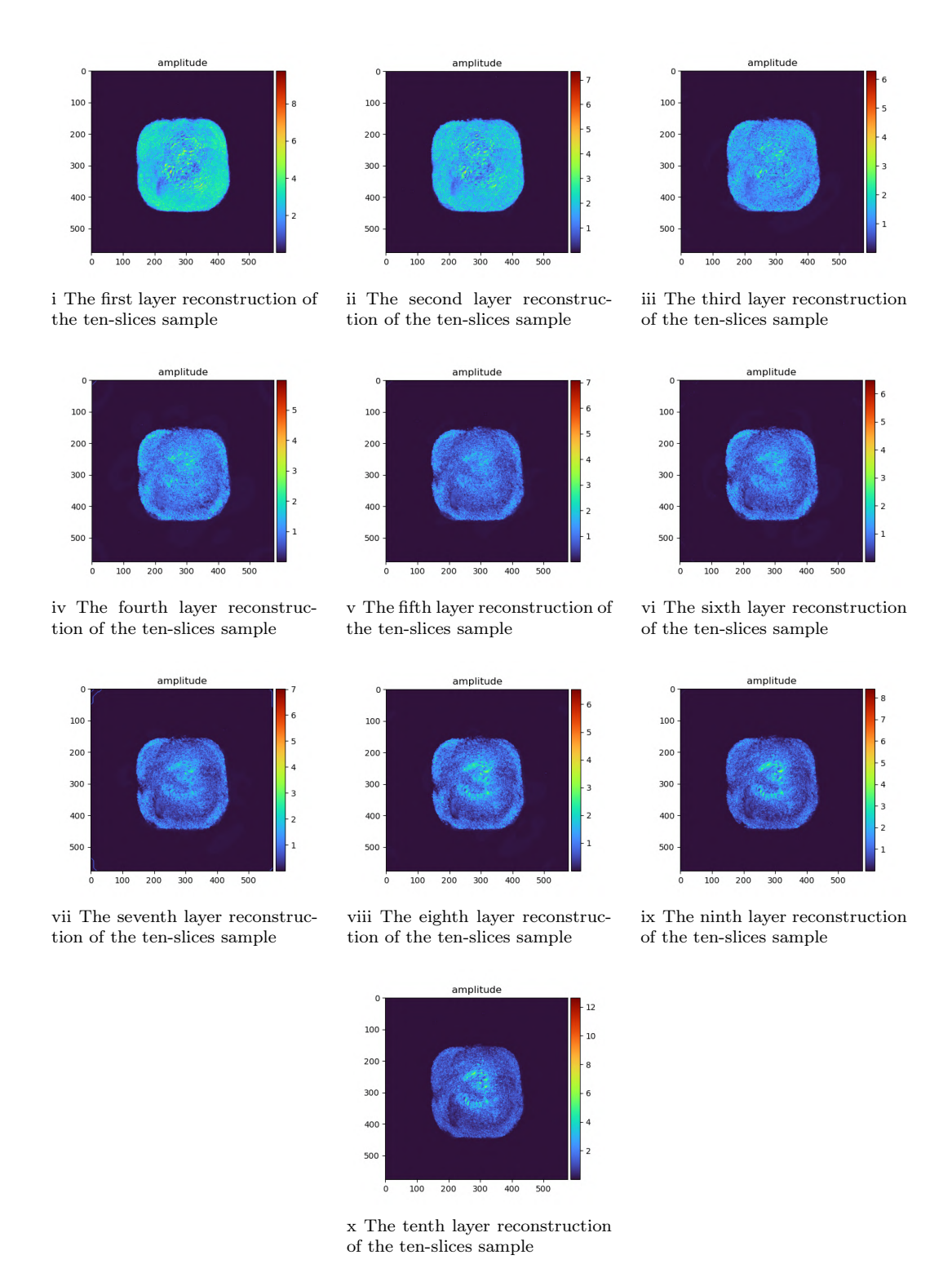


Figure 6.8: Reconstructed pattern of a 10-layer object with a untrainable fine probe. Each layer has a thickness of 60nm and the reconstructions are obtained after 25 epochs of optimizations.

Chapter 7

Conclusion and outlook

7.1 Conclusions

We have built the model of the multi-layer Born approach (MLB). In order to build the model, we derive the formulas. A crucial step is to simplify a sinc function which is responsible for the propagation and the impact of the scattering event in a layer. We have investigated two approaches of simplification in section 3.3: 1. Applying SVD to the sinc function for variable separation. 2. Approximating the sinc function to be 1. The conditions under which the above two simplifications are valid are analyzed. We found that for approach 1, the limitation is the speed of SVD, while for approach 2 is limited by the sampling selection. We further proposed a strategy to build the model by concatenating layers together such that the transmitted and the reflected field becomes the incident field of the next layer in section 3.4. In this process, when the background refractive index differs from one side of the interface to the other side of the interface, we also need to consider the transmission and the reflection at the interface by calculating the Fresnel coefficients. Finally, the model is validated with both simulated and experimental data. It shows that this model demonstrates a high level of accuracy for solving multiple-scattering problem with low or moderate refractive index contrast. Compared with the results of a trust worthy Maxwell solver provided by TU/e, the relative errors at each layer are well limited below 0.12. Also, thanks to the automatic differentiation framework provided by TensorFlow, the process of obtaining the gradient of the refractive index of each layer with respect to a user customized error function is fast and accurate. For any random initial guess, one may expect the result to converge well within 3 iterations. For now, all our reconstructions are based on experiments using visible light, for wavelengths in the EUV and soft X-ray regime, both the lateral and the axial resolution can be further improved.

7.2 Outlook

Encoding model verification. In section 3.5, we only verify the model by a Maxwell solver provided by TU/e. To more rigorously test the model, we are supposed to test the model against more methods, e.g. FEM and RCWA. A good agreement between all these methods may further imply the reliability of the MLB model. Another approach for better validation would be to compare it against canonical objects for which analytical results are available, such as a sphere embedded in a homogeneous medium.

Parameter selection. Recall the formulation of the MLB model, the selection of parameters, e.g. Δz , has huge impact on our final result. Obtaining good results from the algorithm often includes some trial-and-error experiments to find simulation parameters that yield good results. It would be very beneficial to derive a rule of thumb by experimental data and automate the choice of parameters in our algorithm.

Normal vector implementation. Due to the Gibb's phenomena, high contrast problem may not be handled properly in Fourier analysis. The spikes around the discontinuity will not disappear no matter how many spatial harmonics are applied and it is highly related to the severity of the discontinuity. To mitigate the Gibb's phenomena, normal vector field may be a solution to it. But it requires prior knowledge of the object and might be very difficult to calculate. A vector function must be constructed throughout the grid that is normal to all the material interface of the geometry in each layer, which is a priori not known. What is more, the discontinuity of the permittivity distribution prevent us from getting more accurate result in less optimization iterations. In our current algorithm, the reconstruction normally converges after 3 iterations for weakly scattering and thin objects. To improve the speed of convergence, build up a normal vector field by FFF is worthwhile. This implementation of normal vector field can be set as an option in our algorithm. It may be turned on when the contrast is relatively high.

Speed up the program. The computation and memory costs are relatively high as compared to the common used multi-slice (MS) model but lower than finite element (FE) or finite difference time domain (FDTD) methods. To further speed up the program, one needs to decrease the number of Fourier transforms or simplify some calculating process. For instance, when the refractive index does not change between adjacent slices, there is no need to calculate the Fresnel coefficients again.

Automatic differentiation algorithm. In my thesis, the MLB model has been implemented on an open source automatic differentiation framework, TensorFlow. This framework helps to calculate the derivatives by chain rules, thus we do not need to obtain the analytical expressions for object functions in terms of parameters, e.g. samples, probes... The application of this framework may be extended to more electromagnetic models, e.g. RCWA [42, 43]. For further research, one may implement models like RCWA to this framework, the computational speed may increase.

Variable normalization. In MLB model, there are several variables that need to be reconstructed, e.g. samples, probes, propagation distance and more. These variables may have different units and different scales. As we have seen before, for weakly scattering objects, the scattered field is much smaller than the incident field and thus the probe might steer model performance in one direction. Variable normalization might help prevent this situation. Normalization is a data pre-processing tool used to bring the numerical data to a common scale without distorting its shape. It gives equal weights to each variable so that no single variable contributes to most of the model. It is worth to include a normalization process to the program.

Bibliography

- [1] Michael Chen et al. "Multi-layer Born multiple-scattering model for 3D phase microscopy". In: Optica 7.5 (May 2020), p. 394. ISSN: 2334-2536. DOI: 10.1364/optica.383030.
- [2] "moores-law-electronics". In: ().
- [3] "Gordon Moore 1975 Speech". In: ().
- [4] Ray J. Hoobler and Ebru Apak. "Optical critical dimension (OCD) measurments for profile monitoring and control: applications for mask inspection and fabrication". In: 23rd Annual BACUS Symposium on Photomask Technology. Vol. 5256. SPIE, Dec. 2003, p. 638. DOI: 10.1117/12.517931.
- [5] N. G. Orji et al. Metrology for the next generation of semiconductor devices. Oct. 2018. DOI: 10.1038/s41928-018-0150-9.
- [6] Bert Voigtländer. NanoScience and Technology Atomic Force Microscopy Second Edition. Tech. rep. URL: http://www.springer.com/series/3705.
- [7] Roarke Horstmeyer et al. "Diffraction tomography with Fourier ptychography". In: *Optica* 3.8 (Aug. 2016), p. 827. ISSN: 2334-2536. DOI: 10.1364/optica.3.000827.
- [8] Daniel J. Ching et al. "Rotation-as-fast-axis scanning-probe x-ray tomography: the importance of angular diversity for fly-scan modes". In: Appl. Opt. 57.30 (Oct. 2018), pp. 8780–8789. DOI: 10.1364/AO.57.008780. URL: http://www.osapublishing.org/ao/abstract.cfm?URI=ao-57-30-8780.
- [9] A M Maiden, M J Humphry, and J M Rodenburg. Ptychographic transmission microscopy in three dimensions using a multi-slice approach. Tech. rep. 2012.
- [10] Peng Li and Andrew Maiden. "Multi-slice ptychographic tomography". In: Scientific Reports 8.1 (Dec. 2018). ISSN: 20452322. DOI: 10.1038/s41598-018-20530-x.
- [11] T. M. Godden et al. "Ptychographic microscope for three-dimensional imaging". In: Optics Express 22.10 (May 2014), p. 12513. ISSN: 1094-4087. DOI: 10.1364/oe.22.012513.
- [12] Maik Kahnt et al. "Multi-slice ptychography enables high-resolution measurements in extended chemical reactors". In: *Scientific Reports* 11.1 (Dec. 2021). ISSN: 20452322. DOI: 10.1038/s41598-020-80926-6.
- [13] Zhenjiang Xing et al. "Virtual depth-scan multi-slice ptychography for improved three-dimensional imaging". In: Optics Express 29.11 (May 2021), p. 16214. ISSN: 1094-4087. DOI: 10.1364/oe.422214.
- [14] Earl J Kirkland. Advanced Computing in Electron Microscopy Third Edition. Tech. rep.
- [15] J. M. Rodenburg and H. M.L. Faulkner. "A phase retrieval algorithm for shifting illumination". In: Applied Physics Letters 85.20 (Nov. 2004), pp. 4795–4797. ISSN: 00036951. DOI: 10.1063/1.1823034.
- [16] Andrew M. Maiden and John M. Rodenburg. "An improved ptychographical phase retrieval algorithm for diffractive imaging". In: *Ultramicroscopy* 109.10 (Sept. 2009), pp. 1256–1262. ISSN: 03043991. DOI: 10.1016/j.ultramic.2009.05.012.

- [17] A. Schropp et al. "Hard x-ray nanobeam characterization by coherent diffraction microscopy". In: *Applied Physics Letters* 96.9 (2010). ISSN: 00036951. DOI: 10.1063/1.3332591.
- [18] F. Hüe et al. "Wave-front phase retrieval in transmission electron microscopy via ptychography". In: *Physical Review B Condensed Matter and Materials Physics* 82.12 (Sept. 2010). ISSN: 10980121. DOI: 10.1103/PhysRevB.82.121415.
- [19] Jacob Seifert et al. "Efficient and flexible approach to ptychography using an optimization framework based on automatic differentiation". In: OSA Continuum 4.1 (Jan. 2021), p. 121. ISSN: 2578-7519. DOI: 10.1364/osac.411174.
- [20] H P Urbach. Advanced Photonics AP3382. Tech. rep. 2021.
- [21] https://empossible.net/academics/emp5337/.
- [22] Raymond B. Cattell. "The Scree Test For The Number Of Factors". In: Multivariate Behavioral Research 1.2 (1966). PMID: 26828106, pp. 245-276. DOI: 10.1207/s15327906mbr0102\
 _10. eprint: https://doi.org/10.1207/s15327906mbr0102_10. URL: https://doi.org/10.1207/s15327906mbr0102_10.
- [23] Matan Gavish and David L. Donoho. "The optimal hard threshold for singular values is $4/\sqrt{3}$ ". In: *IEEE Transactions on Information Theory* 60.8 (2014), pp. 5040–5053. ISSN: 00189448. DOI: 10.1109/TIT.2014.2323359.
- [24] Svante Wold and Models Svante Wold. Cross-Validatory Estimation of the Number of Components in Factor and Principal Components Models Cross-Validatory Estimation of the Number of Components in Factor and Principal Components. Tech. rep. 4. 1978, pp. 397–405.
- [25] Peter D Hoff. Model averaging and dimension selection for the singular value decomposition. Tech. rep. 2006. URL: http://www.stat.washington.edu/hoff/...
- [26] Art B. Owen and Patrick O. Perry. "Bi-cross-validation of the SVD and the nonnegative matrix factorization". In: *Annals of Applied Statistics* 3.2 (Mar. 2009), pp. 564–594. ISSN: 19326157. DOI: 10.1214/08-AOAS227.
- [27] Steven Goldenberg, Andreas Stathopoulos, and Eloy Romero. A GOLUB-KAHAN DAVID-SON METHOD FOR ACCURATELY COMPUTING A FEW SINGULAR TRIPLETS OF LARGE SPARSE 2 MATRICES. Tech. rep.
- [28] Dan Teng and Delin Chu. "A Fast Frequent Directions Algorithm for Low Rank Approximation". In: *IEEE Transactions on Pattern Analysis and Machine Intelligence* 41.6 (June 2019), pp. 1279–1293. ISSN: 19393539. DOI: 10.1109/TPAMI.2018.2839198.
- [29] Ph.D Niku Ekhtiari. Comparing Ground Truth With Predictions Using Image Similarity Measures. https://up42.com/blog/tech/image-similarity-measures. Jan. 2021.
- [30] R.J. Dilz. "A spatial spectral domain integral equation solver for electromagnetic scattering in dielectric layered media". English. Proefschrift. PhD thesis. Electrical Engineering, Nov. 2017. ISBN: 978-946233-774-9.
- [31] Mark van de Kerkhof et al. "High-power EUV lithography: spectral purity and imaging performance". In: Journal of Micro/Nanolithography, MEMS, and MOEMS 19.03 (Sept. 2020). ISSN: 19325134. DOI: 10.1117/1.jmm.19.3.033801.
- [32] Brian Abbey et al. "Lensless imaging using broadband X-ray sources". In: *Nature Photonics* 5.7 (July 2011), pp. 420–424. ISSN: 17494885. DOI: 10.1038/nphoton.2011.125.
- [33] Pierre Thibault and Andreas Menzel. "Reconstructing state mixtures from diffraction measurements". In: *Nature* 494.7435 (Feb. 2013), pp. 68–71. ISSN: 00280836. DOI: 10.1038/nature11806.
- [34] Xiaowen Shi et al. "Multi-modal ptychography: Recent developments and applications". In: Applied Sciences (Switzerland) 8.7 (June 2018). ISSN: 20763417. DOI: 10.3390/app8071054.

- [35] Xukang Wei and Paul Urbach. "Ptychography with multiple wavelength illumination". In: Optics Express 27.25 (Dec. 2019), p. 36767. ISSN: 10944087. DOI: 10.1364/oe.27.036767.
- [36] Alden S. Jurling and James R. Fienup. "Applications of algorithmic differentiation to phase retrieval algorithms". In: *J. Opt. Soc. Am. A* 31.7 (July 2014), pp. 1348–1359. DOI: 10. 1364/JOSAA.31.001348. URL: http://www.osapublishing.org/josaa/abstract.cfm? URI=josaa-31-7-1348.
- [37] Youssef S.G. Nashed et al. "Distributed Automatic Differentiation for Ptychography". In: *Procedia Computer Science*. Vol. 108. Elsevier B.V., 2017, pp. 404–414. DOI: 10.1016/j.procs.2017.05.101.
- [38] Woutjan Branderhorst et al. Ordered subsets algorithms for transmission tomography Pixel-based subsets for rapid multi-pinhole SPECT reconstruction Ordered subsets algorithms for transmission tomography. Tech. rep. 1999, pp. 2835–2851.
- [39] Ulugbek S. Kamilov et al. "Learning approach to optical tomography". In: Optica 2.6 (June 2015), p. 517. ISSN: 2334-2536. DOI: 10.1364/optica.2.000517.
- [40] Leonid I Rudin, Stanley Osher, and Emad Fatemi. Nonlinear total variation based noise removal algorithms*. Tech. rep. 1992, pp. 259–268.
- [41] Paul Rodríguez. Total variation regularization algorithms for images corrupted with different noise models: A review. 2013. DOI: 10.1155/2013/217021.
- [42] Shane Colburn and Arka Majumdar. "Inverse design and flexible parameterization of meta-optics using algorithmic differentiation". In: *Communications Physics* 4.1 (Dec. 2021). ISSN: 23993650. DOI: 10.1038/s42005-021-00568-6.
- [43] Ziwei Zhu and Changxi Zheng. "Differentiable scattering matrix for optimization of photonic structures". In: *Optics Express* 28.25 (Dec. 2020), p. 37773. ISSN: 10944087. DOI: 10.1364/oe.409261.
- [44] Brenden P. Epps and Eric M. Krivitzky. "Singular value decomposition of noisy data: noise filtering". In: *Experiments in Fluids* 60.8 (Aug. 2019). ISSN: 14321114. DOI: 10.1007/s00348-019-2768-4.

Appendix A

Optimal truncation method

Optimal truncation method. Here we present the optimal truncation method which works well for noisy data. Suppose the measured noisy matrix Y obeying

$$Y = X + \sigma Z,\tag{A.0.1}$$

where the noise matrix Z has an independent, zero-mean distribution with a noise level of σ and the matrix X is the noise-free data. Matan Gavish [44] has found that a Gaussian zero-mean distributed noise matrix usually has singular values showed as red line in Fig. A.1 and its corresponding noisy measurement has a singular values distribution as the green line in Fig. A.1. As long as we truncate the singular values smaller than the maximum singular value of noise matrix, only signal information will be contained.

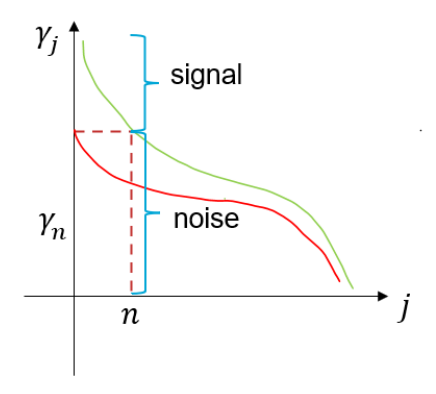


Figure A.1: optimal SVD truncation. Plot the singular value vectors of both noise data (red line) and noisy measurement (green line). Truncate the singular values of the measurements data smaller than the largest singular value of noise data, only signal information will be contained.

```
\% add noise to the original data dz = lambda; sigma = 1; y = sinc(dk*dz/2); Xnoisy = y + sigma * randn(size(y)); N = size(Xnoisy, 1); cutoff = (4/sqrt(3)) * sqrt(N) * sigma; % Hard threshold r = max(find(diag(S_noisy) > cutoff)); % keep modes w/sig > cutoff % noise data SVD [U\_noisy, S\_noisy, V\_noisy] = svd(Xnoisy); Xclean = U\_noisy(:,1:r) * S\_noisy(1:r,1:r) * V\_noisy(:,1:r) ';
```

Listing A.1: Matlab code for the optimal truncation method

Add a Gaussian zero-mean distributed noise to $S(\rho', \rho)$, the noise level σ adding to the original clean data is 1. Fig.(A.2i - A.2ii) show the original clean $S(\rho', \rho)$ and the noisy $S(\rho', \rho)$, respectively. One can hardly tell the basic pattern from the noisy data and discontinuities are introduced due to the noise. Also, the magnitude difference between the clean and noisy data cannot be ignored.

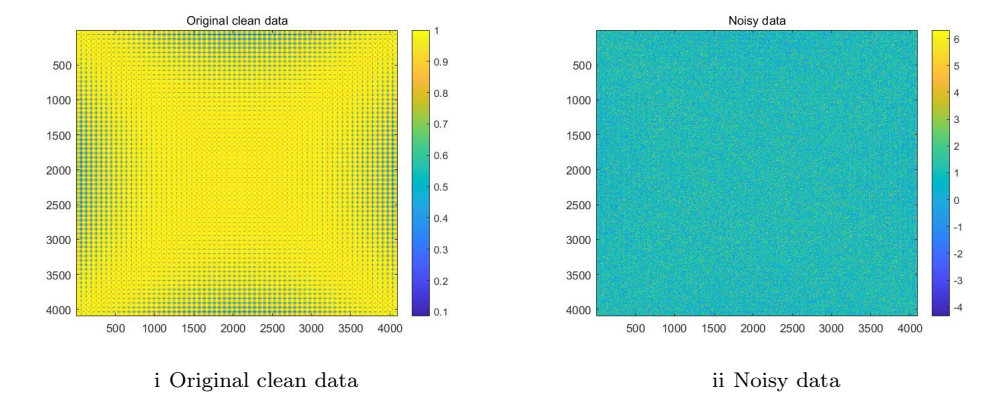


Figure A.2: Add noise to $S(\rho', \rho)$. The left subfigure demonstrates the distribution of original clean data and the right subfigure shows the pattern of the noisy data. The sinc function pattern can hardly be teller from the figure.

Then we apply optimal truncation code to reconstruct the clean data by performing optimal singular value decomposition. Fig.(A.3) depicts the reconstructed clean $S(\rho', \rho)$. It's obvious that the reconstructed clean data has better quality than the noisy data. The basic pattern is recognizable and the magnitude difference with the real pattern is within an acceptable range.

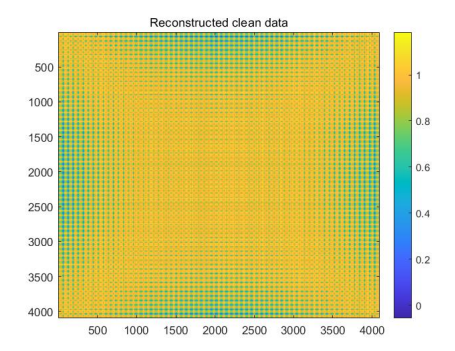
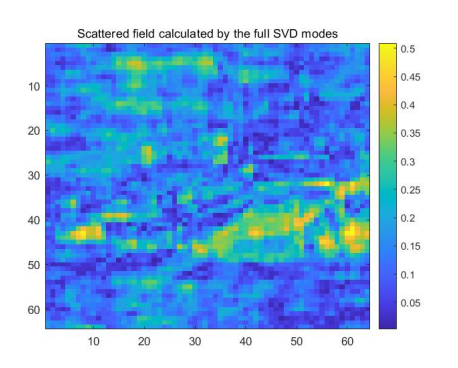
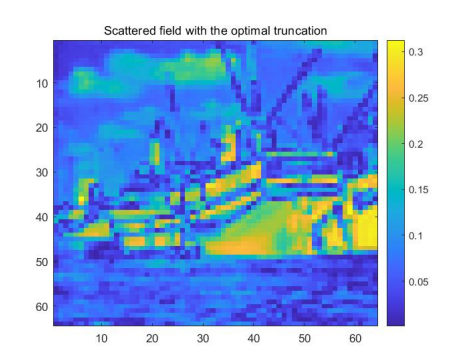


Figure A.3: Reconstructed clean $S(\rho', \rho)$

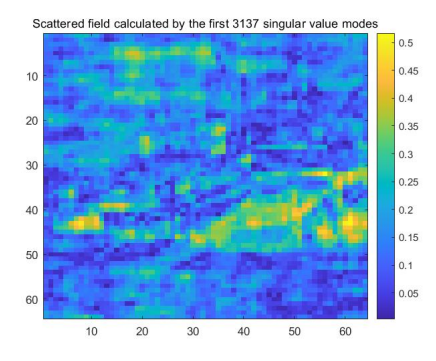
To reconstruct the clean $S(\rho', \rho)$ as shown in Fig. A.3, only the first two singular modes have been applied, which is identical to the result obtained by the energy accumulation method. To check the reliability of the optimal truncation method, we here calculate the scattered field by using the reconstructed clean data and the noisy data as depicted in Fig. A.4i - A.4ii, respectively.





i Scattered field with full noisy data components

ii Scattered field with the optimal truncation



iii Scattered field with the energy accumulation truncation $\,$

Figure A.4

One may see clearly from the figures that the first singular mode of $S(\rho', \rho)$ only is capable of estimating the scattered waves for weakly scattering objects. Also, one may notice that the estimated scattered field is smooth and almost all the speckles and discontinuous area are disappeared. Thus we may guess that the information of the sudden changes of the contrast permittivity distributions are contained in the small singular value modes. To further verify our ideas, we calculate the scattered field with the noisy $S(\rho', \rho)$ term and perform the energy accumulation SVD truncation method to it. According to Fig.(A.5), it requires 3137 modes to capture 95% of the sinc term energy. And Fig. A.4iii shows that the energy accumulation truncation method keeps most of the large permittivity contrast information.

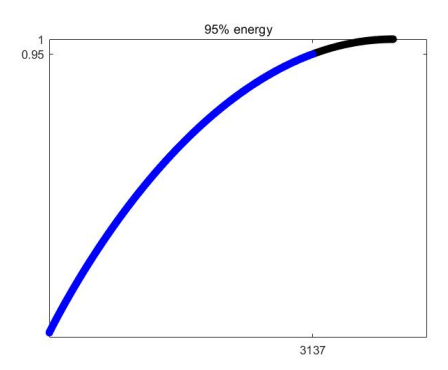
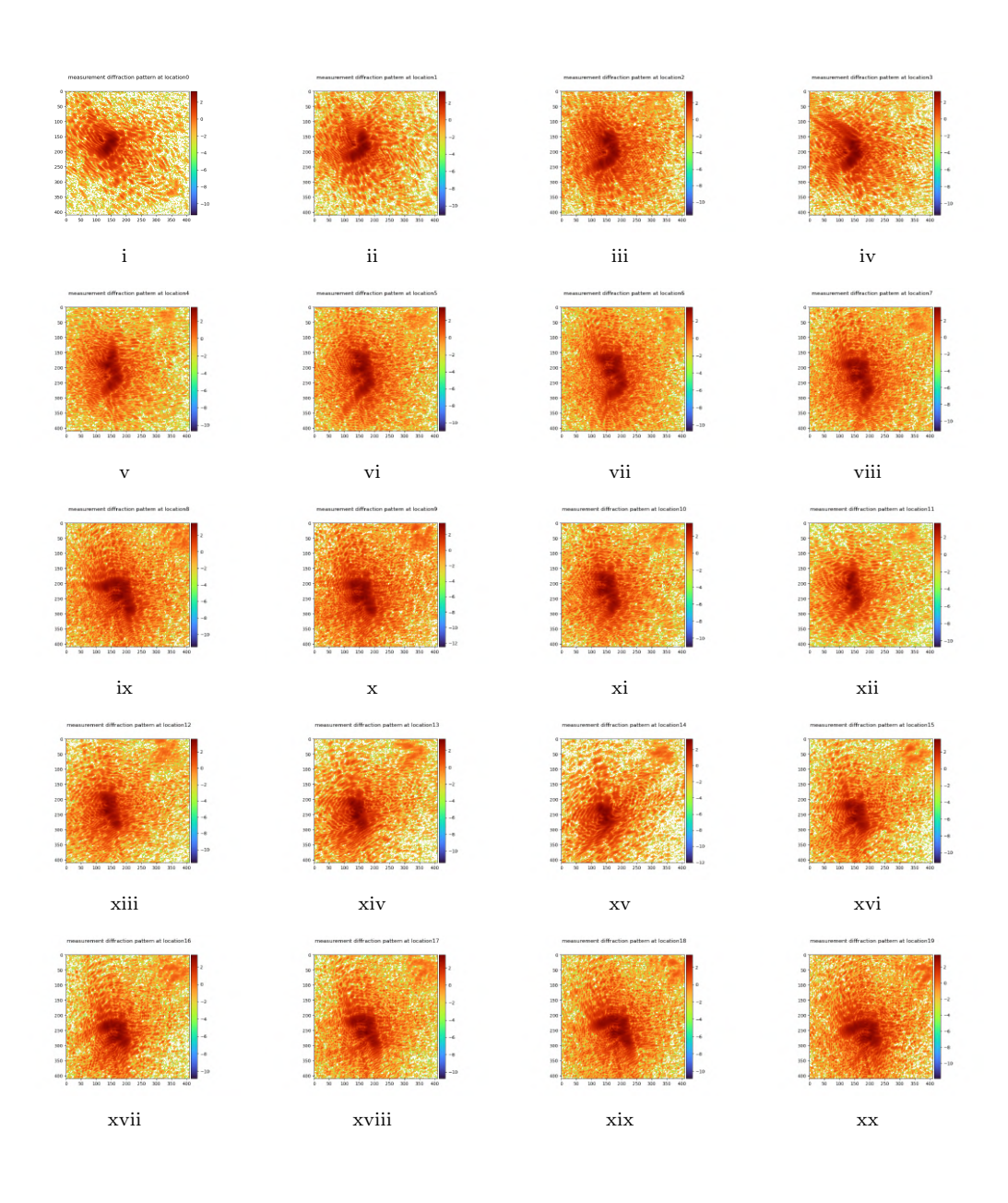
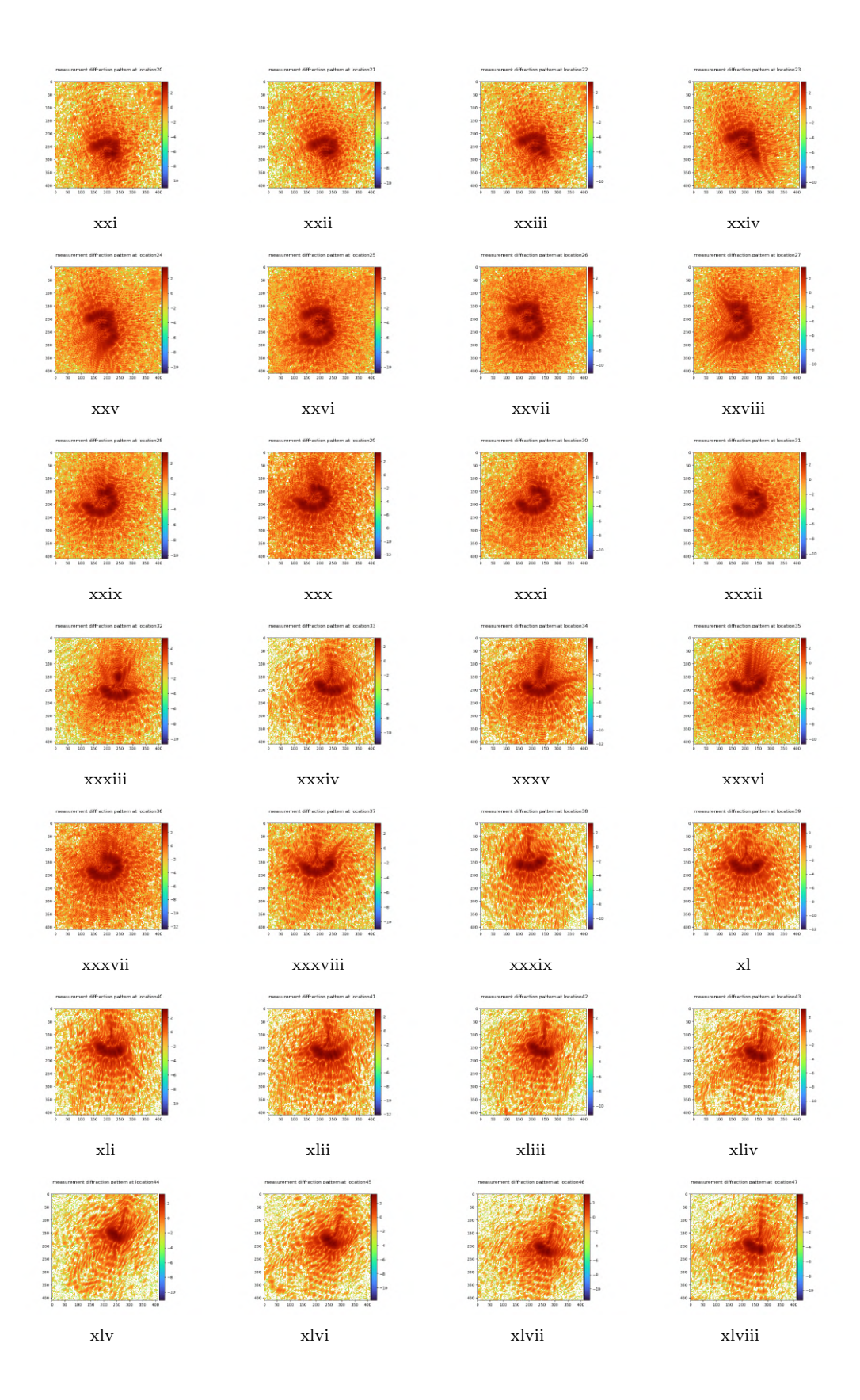


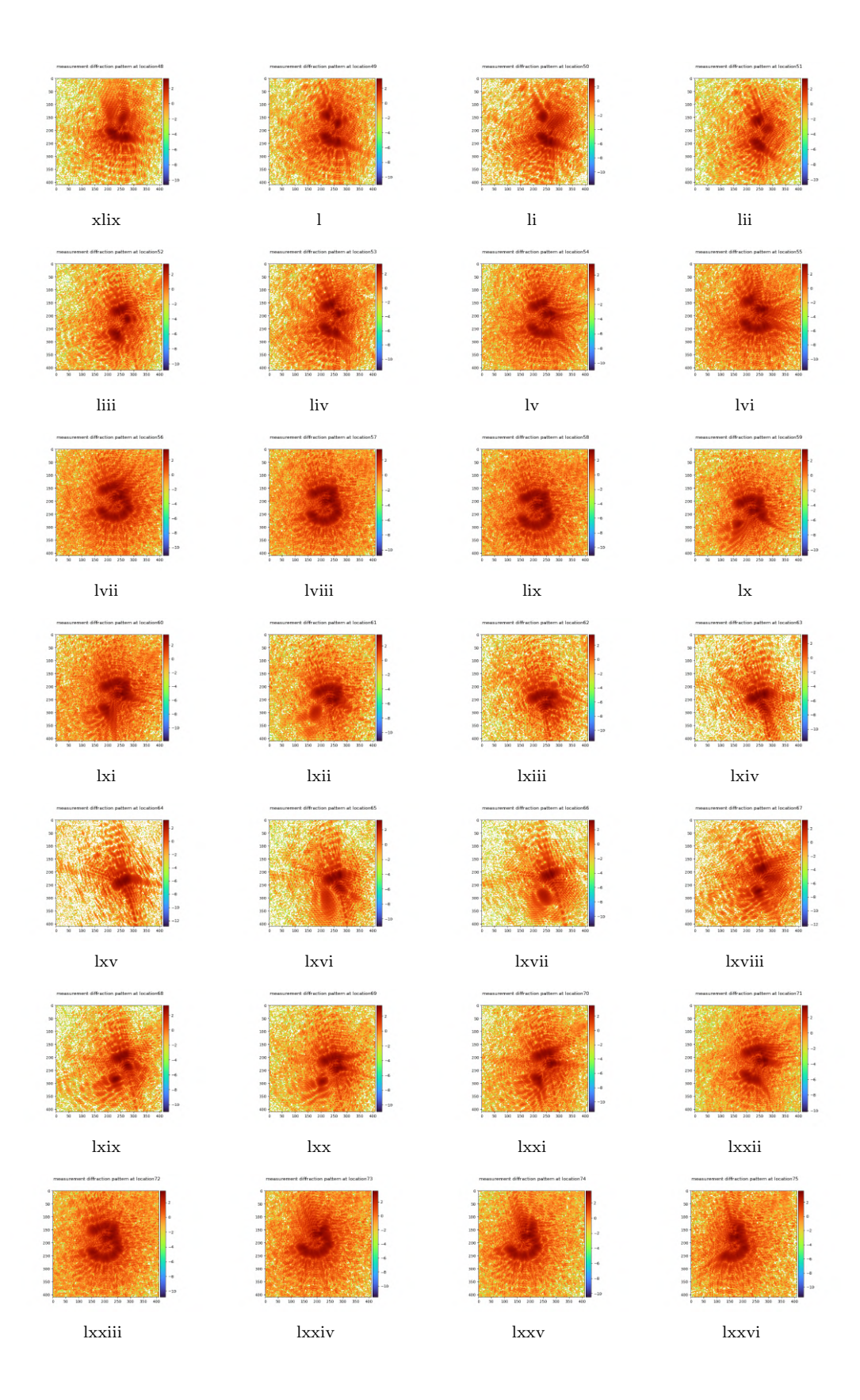
Figure A.5: Black line represents how singular-modes contribute to the total energy of noisy $S(\rho', \rho)$. Blue line indicates the modes required to capture 95% energy of noisy $S(\rho', \rho)$.

Appendix B

Diffraction pattern measurements







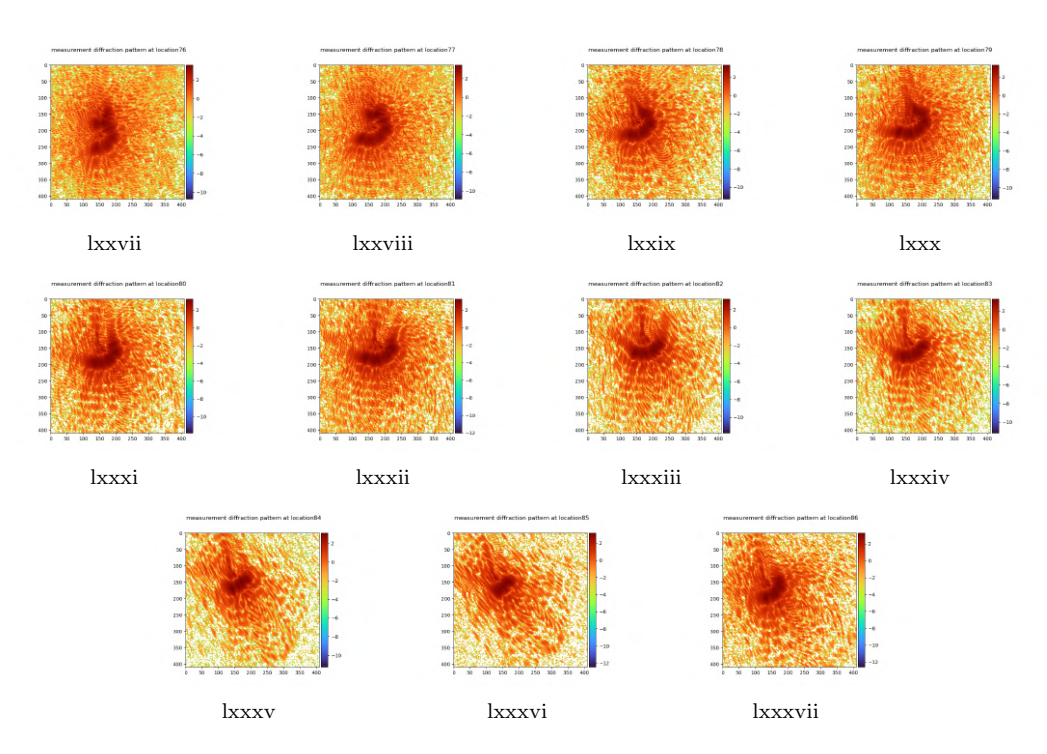
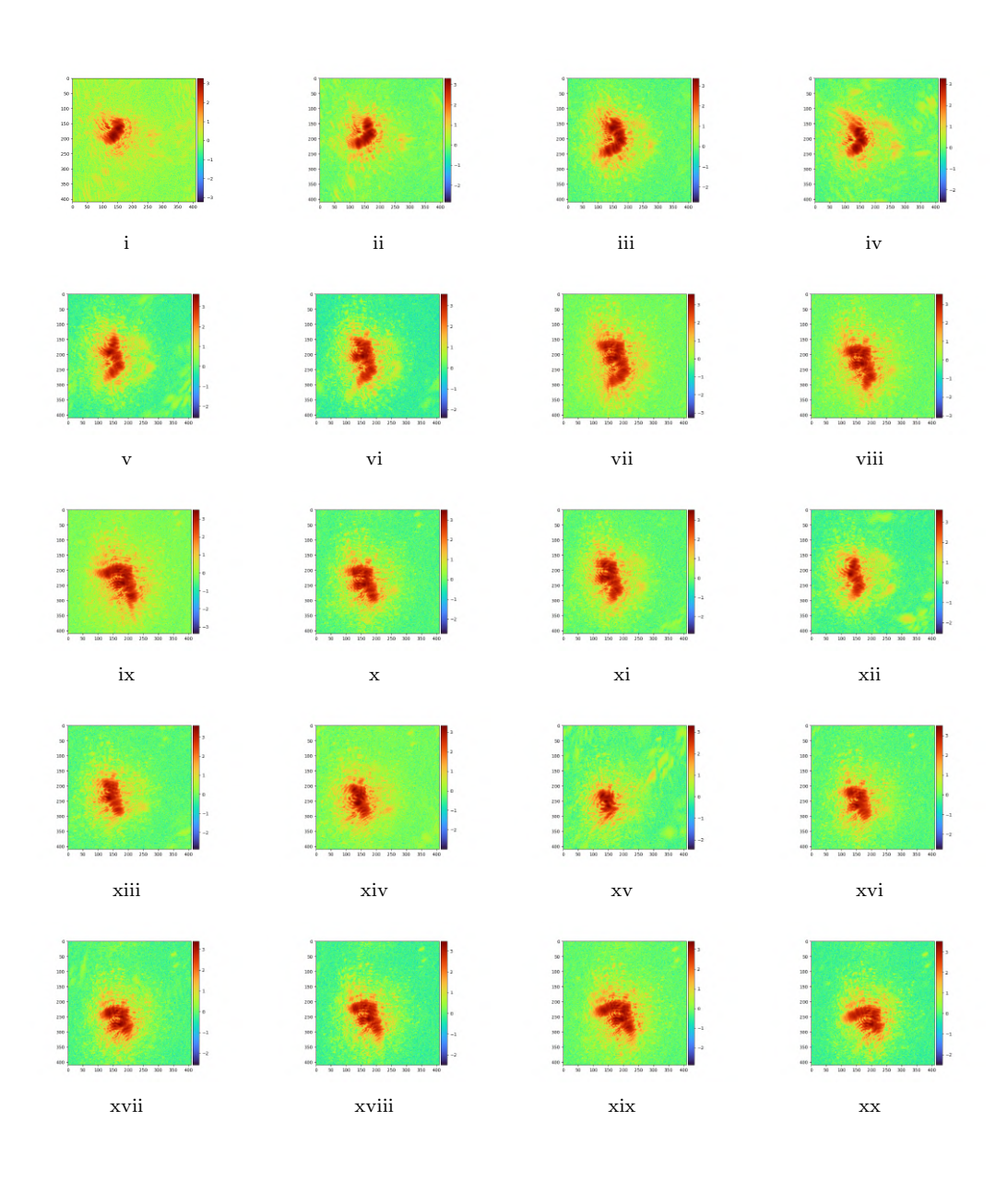
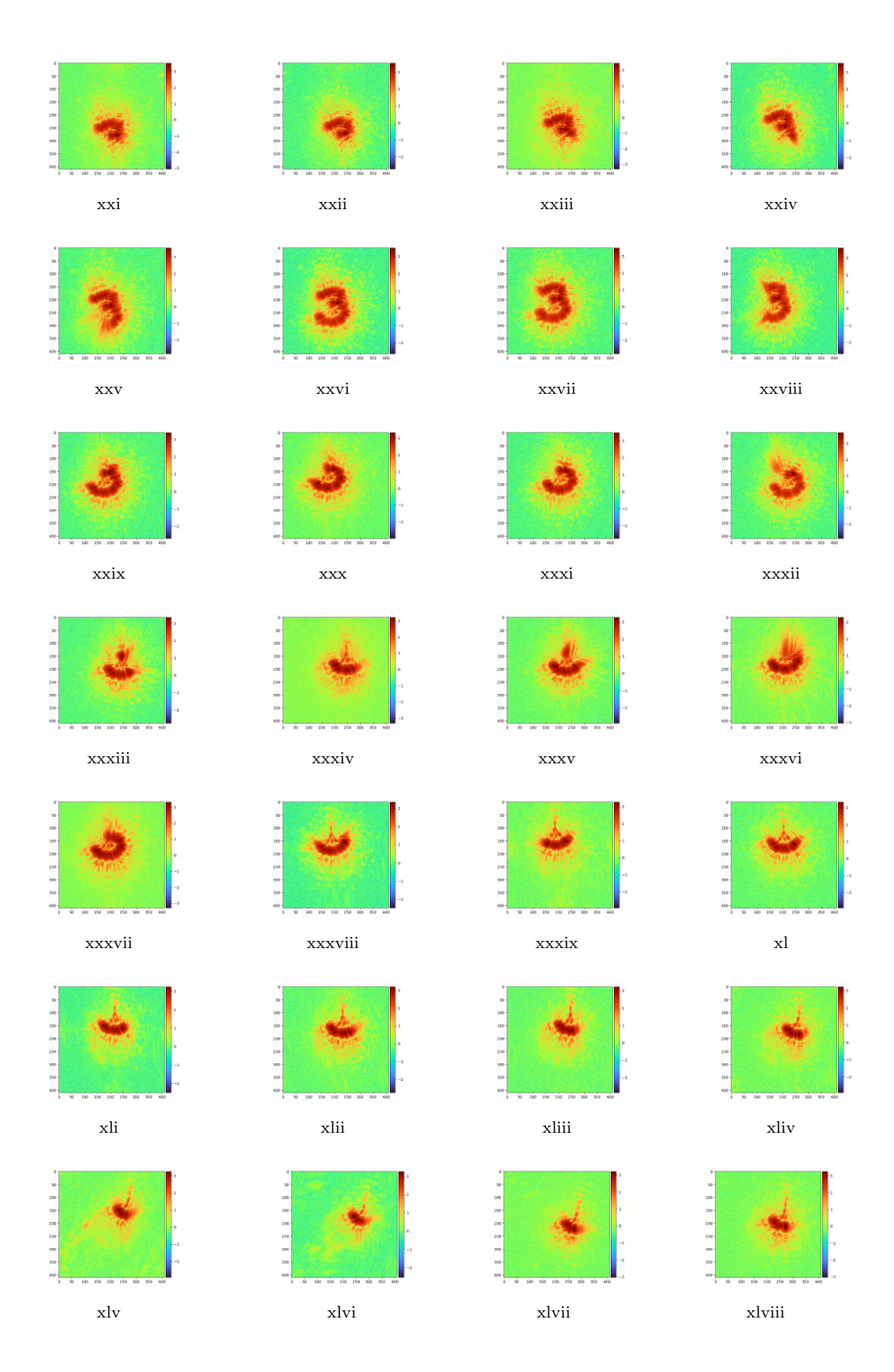


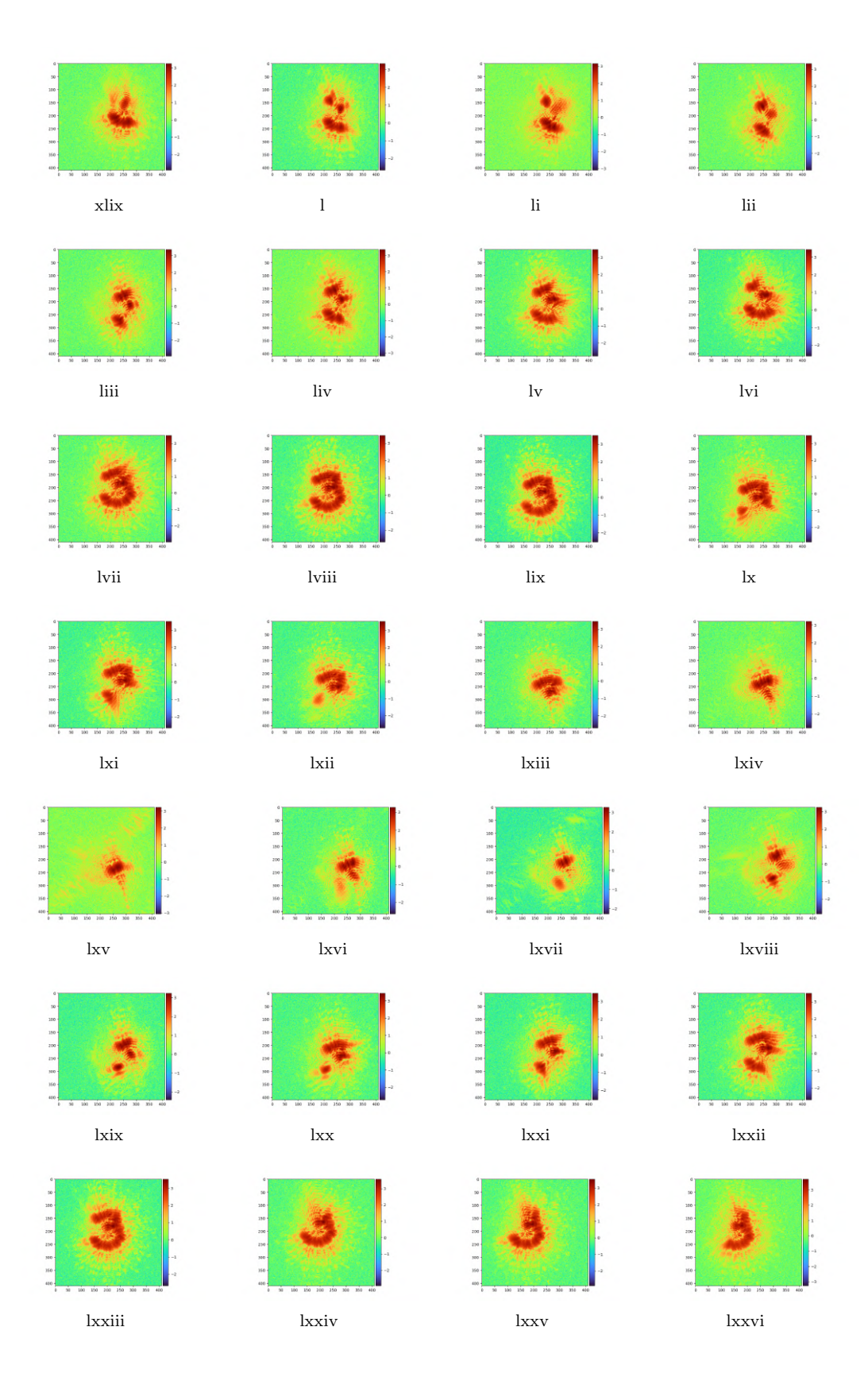
Figure B.0: Measurement diffraction patterns at different scan locations

Appendix C

Diffraction pattern predictions







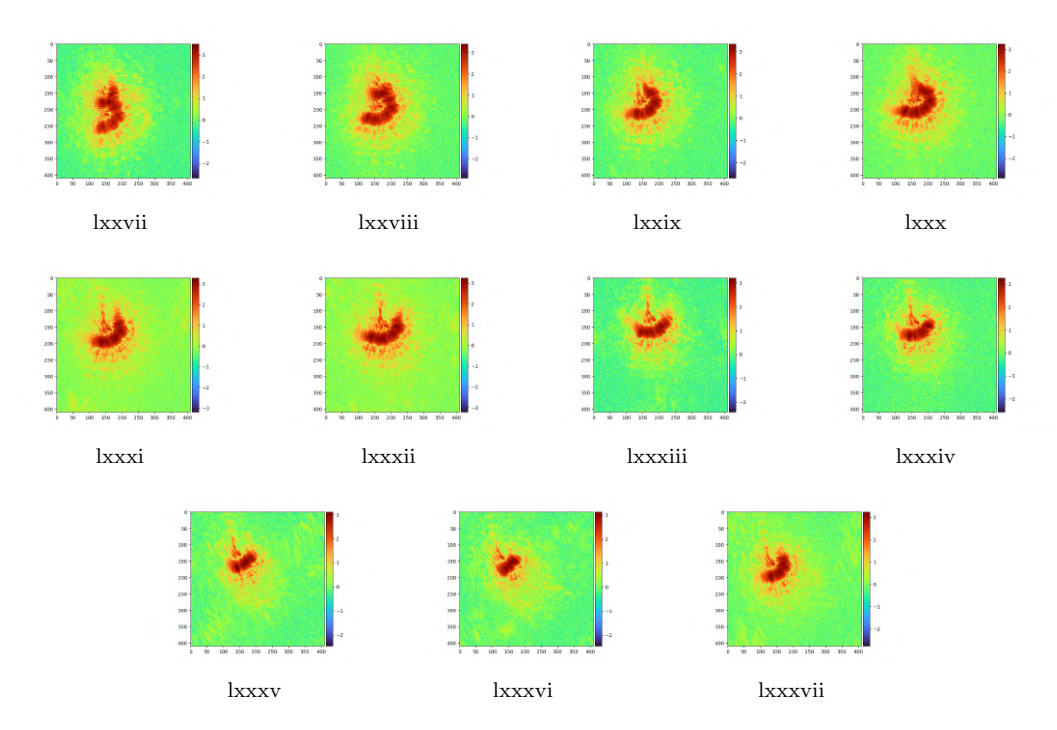


Figure C.0: Diffraction pattern predictions at different scan locations with $\Delta z = 600 \mathrm{nm}$